We are IntechOpen, the world's leading publisher of Open Access books
Built by scientists, for scientists

4,800
Open access books available

122,000
International authors and editors

135M
Downloads

Our authors are among the

154
Countries delivered to

TOP 1%
most cited scientists

12.2%
Contributors from top 500 universities

WEB OF SCIENCE™

Selection of our books indexed in the Book Citation Index
in Web of Science™ Core Collection (BKCI)

Interested in publishing with us?
Contact book.department@intechopen.com

Numbers displayed above are based on latest data collected.
For more information visit www.intechopen.com

UWB in Medicine – High Performance UWB Systems for Biomedical Diagnostics and Short Range Communications

Dayang Lin, Michael Mirbach, Thanawat Thiasiriphet, Jürgen Lindner, Wolfgang Menzel, Hermann Schumacher, Mario Leib and Bernd Schleicher

1. Introduction

This chapter presents scientific achievements in the field of UWB radar and communication systems for biomedical applications. These contributions focus on low-power MMIC designs, novel antenna structures and competitive approaches for communication and imaging.

The first section describes components for UWB radar sensors and communication systems, namely antennas and integrated circuits. Novel broadband antenna concepts for UWB radar and communication applications are presented. Symmetrical UWB antenna structures for free space propagation with improved performance compared to existing antennas regarding radiation pattern stability over frequency are designed, realized and successfully characterized. Novel differential feeding concepts are applied, suppressing parasitic radiation by cable currents on feed lines. For applications such as communication with implants and catheter localization, a miniaturized antenna optimized for radiation in human tissue is designed. The radiation characteristics of the antenna are measured using an automated setup embedded in a liquid consisting of sugar and water, mimicking the dielectric properties of biological tissue. For UWB radar transmitters, a differential and low-power impulse generator IC is realized addressing the FCC spectral mask based on a quenched cross-coupled LC oscillator. The total power consumption is only 6 mW at an impulse repetition rate of 100 MHz. By adding a simple phase control circuit setting the start-up phase condition of the LC oscillator, an impulse generator with a bi-phase modulation scheme is achieved. A further modification introduces a variable width of the pulse envelope as well as a variable oscillation frequency. The corresponding spectra have controllable 10 dB bandwidths and center frequencies fitting the different spectral allocations in the USA, Europe and Japan. On the receiver side, both a fully differential correlation-based and an energy detection receiver for the 3.1-10.6 GHz band are designed. Monostatic UWB radar systems require

transmit/receive turn-around times in the nanosecond regime. Integrated front-ends which successfully address this issue are presented here for the first time.

The second section deals with signal processing. As, due to the large RF bandwidth, direct analog to digital conversion and digital signal processing are not feasible (at least not at reasonable power consumption), analog signal processing is one focus. For communication, detection methods based on analog correlation require channel estimation, storing of impulse responses and also precise time synchronization. Therefore methods based on energy detection are developed which require no or little channel knowledge, having low complexity, robustness to multipath propagation and high resistance to synchronization and symbol clock errors. New modulation techniques are described, which can cope with interchip and intersymbol interference. Also a novel support by a comb filter resulting in significant SNR improvements in interference and multiuser scenarios is presented. The methods developed for communication applications can also be used in the radar context. For detection and tracking of moving targets (e.g. heart in the body) new algorithms based on particle filtering are developed for the digital signal processing part. It is shown that the accuracy, the resolution and robustness can be improved compared to conventional methods. For the objective of catheter localization, the knowledge of the shape and position of the human body surface is inevitable. A UWB imaging algorithm for the detection and estimation of this surface has been developed based on trilateration and is also described in this second section. Furthermore, building on this surface estimation algorithm, a new method for the localization of transmitters in dielectric media is presented. Taking into account the refraction effects on the boundary surface, the algorithm uses the impulse time of arrival to determine the transmitter position inside of the dielectric medium.

The third section finally describes the design of bistatic UWB radar systems using the components presented in the first section. Single-ended and differential radar demonstrators are developed, with which the potential of impulse-radio UWB sensing is evaluated. Measurements aimed at applications of the developed hardware such as vital sign monitoring and communication with implants are presented. Further measurements are performed to prove the functionality of the imaging algorithms derived in the second section. For surface estimation, a single radar sensor is moved around a highly reflective target in order to emulate a whole sensor array. For the verification of subsurface transmitter localization, a transmitter is placed inside of a container filled with tissue mimicking liquid, and its position is visualized with respect to the estimated container surface.

2. Circuit and component design

2.1. UWB antennas

Concepts for antennas with an ultra-wideband behavior are well-known and established [30]. However, advancements focusing on specific applications and specific performance parameters are inevitable to keep pace with the requirements of modern communication, radar, and localization systems. In particular in the medical environment, application-oriented antennas are mandatory to cope with the need for reliable systems (e.g. health monitoring systems) or with extreme environmental conditions (e.g. implanted systems). In the following, three novel UWB antennas are introduced targeting different tasks in the medical field and showing outstanding characteristics with respect to certain key antenna parameters.

## 2.1.1. Circular slot antenna excited with a dipole element
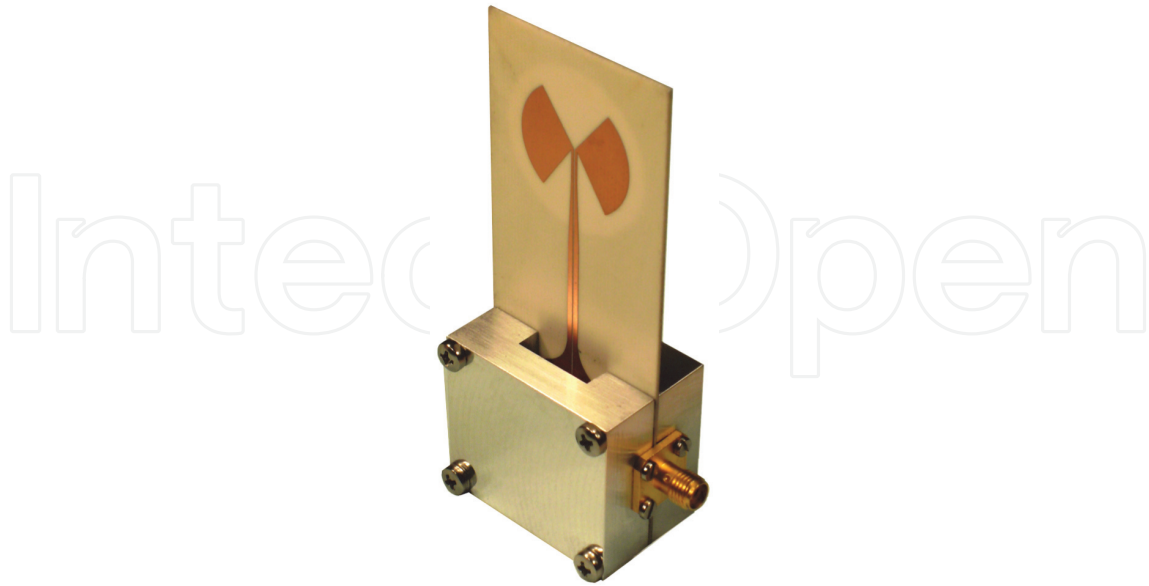
Figure 1. Dipole slot antenna.

Planar broad monpoles or dipoles are favored UWB antennas for communication systems with high data rates, e. g. potentially used in base stations for patient monitoring. However, broad monopoles fed single-endedly are prone to cable currents on the feeding line disturbing the radiation characteristic in the lower frequency range [15], while dipoles behave like a λ-radiator with a zero in main beam direction in the upper frequency range. Both effects lead to an undesired change of the radiation pattern in the operational frequency range reducing the effective bandwidth. For the widely-used impulse based UWB systems, this leads to a broadening of the impulse and consequently to a degraded system performance.

A practical solution to overcome the described parasitic radiation pattern performance is the combination of a circular slot antenna with a dipole feeding element as depicted in Fig. 1. The circular slot behaves like a broad monopole according to Babinet's principle. A broad dipole located in the center of the circular slot and consisting of two circular segments excites the slot antenna. The inherent symmetrical feeding of the dipole avoids the propagation of cable currents due to the virtual ground plane in between the transmission lines and results in an uniform radiation characteristic over the UWB frequency range.

The length of the exciting dipole is designed to be $\lambda/2$ at the center of the FCC UWB frequency range. Therefore, the dipole is smaller than pure UWB dipole antennas with a typical length of $\lambda/2$ at the lower edge of the FCC UWB frequency range. The perimeter of the circular slot is about λ at the lower edge of the FCC UWB frequency range leading to a resonance at 4.3 GHz (see simulation result for $|S_{11}|$ in Fig. 2(a)), and hence, to a return loss better than 10 dB at 3.1 GHz. Additional resonances with a low qualtiy factor are arising if the perimeter of the slot is a multiple of the wavelength (see at 6.9 GHz and 9.8 GHz in Fig. 2(a)). Therefore, a UWB behavior regarding return loss is achieved.

In order to characterize the dipole slot antenna with a single-ended coaxial line, a common UWB planar transition from coplanar stripline to a microstrip line based on [32] is used. A metallic shielding around this balun suppresses any parasitic radiation (see Fig. 1). The

(a) Reflection coefficient

(b) Measured radiation pattern in dB (E-plane)
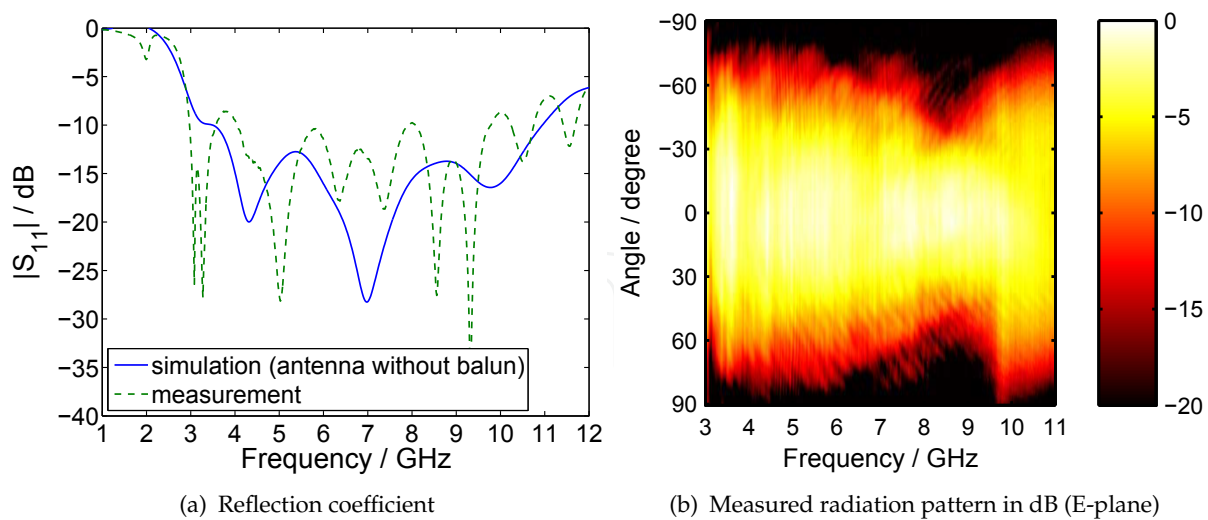
Figure 2. Reflection and radiation performance of the dipole slot antenna.

measured return loss behavior of the antenna including balun is presented in Fig. 2(a) and shows the predicted UWB performance.

The measured radiation pattern demonstrates the desired uniform characteristic over the FCC frequency range, as can be seen in Fig. 2(b) for the E-plane. In the H-plane a similar pattern is obtained having a slightly narrower beam with a mean 3 dB beamwidth of 60° in contrast to 65° for the E-plane. The uniform radiation behavior in the frequency domain results in a short antenna impulse response making the antenna a suitable candidate for impulse-based communication systems.

An upgrade of this single polarized antenna for horizontal and vertical polarizations is possible, if two narrow feeding dipoles are placed in orthogonal position to each other inside the circular slot. The expense of the additional feature is a deterioration in the return loss and radiation characteristic (see [20]).
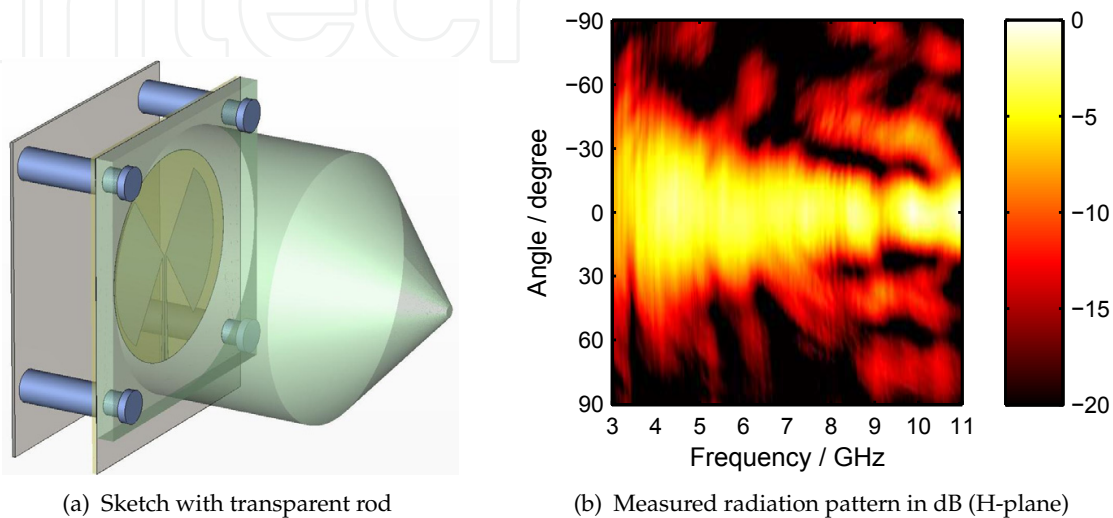
2.1.2. Dielectric rod antenna fed by a planar circular slot

Emerging applications in medicine are vital sign monitoring [33], breast cancer detection [11], and tracking of inner organs for improved magnetic resonance tomography [38]. For these radar based sensing systems, directive antennas with a small beamwidth in both planes are compulsory. A promising approach to achieve this attribute is to exploit dielectric rod antennas either fed by a tapered slot antenna [14] or by a biconical dipole [4]. Both ideas show very good electrical characteristics, but suffer from necessary sophisticated fabrication and assembly.

A new antenna proposal is shown in Fig. 3(a). In this concept, the planar circular slot antenna presented in Sec. 2.1.1 acts as feed for a circular dielectric waveguide. The electrical field distribution inside the circular slot is similar to the fundamental mode H_{11} of the dielectric waveguide. Hence, this mode is predominantly excited. Due to that and since the H_{11}-mode possesses no cutoff frequency, in general an ultra-wideband performance is obtained. The diameter of the dielectric rod is chosen to 43 mm, which is a compromise between a good return loss behavior and single-mode operation of the dielectric waveguide. The conical shape

at the end of the rod acts as smooth transition of the waveguide impedance to the free space impedance.

Due to the rod permittivity of 2.8, the electromagnetic field is mainly concentrated within the rod. Therefore, the antenna primarily radiates in forward direction along the rod. The unidirectionality and, hence, the gain is slightly improved – especially for lower frequencies – placing a metallic reflector at the backside of the antenna (see Fig. 3(a)). The reflector distance for the shown structure is $\lambda/4$ at 5.35 GHz leading to an optimized mean gain.

(a) Sketch with transparent rod   (b) Measured radiation pattern in dB (H-plane)

Figure 3. Sketch and radiation performance of the dielectric rod antenna fed by the dipole slot antenna.

The radiation pattern in Fig. 3(b) shows the obtained small beamwidth of the antenna for the H-plane. The increased side lobe level at frequencies above 8 GHz is caused by a parasitic leaky wave and is hardly avoidable for rod antennas. The given radiation characteristics in Fig. 3(b) are typical for both planes and results in a high mean gain of 8.7 dBi including the return loss. Due to the fact that the return loss is better than 10 dB from 3.5 GHz to 11.8 GHz, the influence of the return loss on the realized gain is negligible.

Besides this good electrical performance, the major benefits of this antenna in contrast to [14] and [4] are the compactness, the low weight, and the ease of fabrication. These attributes make the antenna also interesting for all kinds of industrial applications.

2.1.3. UWB slot antenna optimized for radiation in human tissue

High data rate communication for implanted devices [5] or precise catheter localization inside the human body are futuristic topics in medicine. There, impulse-based UWB technology is advantageous compared to narrow band systems due to the low power consumption caused by the simple system architecture. However, UWB antennas optimized for radiation in human tissue are hardly investigated.

In Fig. 4(a) a UWB antenna is proposed for radiation in human tissue, which is based on a similar concept as the dipole slot antenna in Sec. 2.1.1. An elliptical slot antenna is fed by a broad monopole located in the center of the slot. A monopole is chosen to obtain a small structure and to avoid a bulky balun for characterization purposes. Instead of a single layer

structure, two substrate layers with slots in the top and bottom layer metalizations are used. The monopole is arranged in the center metalization layer and is fed by a triplate line. In this way, the buried feeding is insulated from the adjacent highly lossy human tissue. The antenna dimensions need to be optimized according to the surrounding medium of the antenna. The width of the antenna is 11 mm assuming skin tissue around the antenna with a typical permittivity of 28 at 6.85 GHz. The size reduction factor compared to an antenna designed for air instead of skin tissue is 5.4 leading automatically to a miniaturized UWB antenna.

(a) Sketch   (b) Photograph
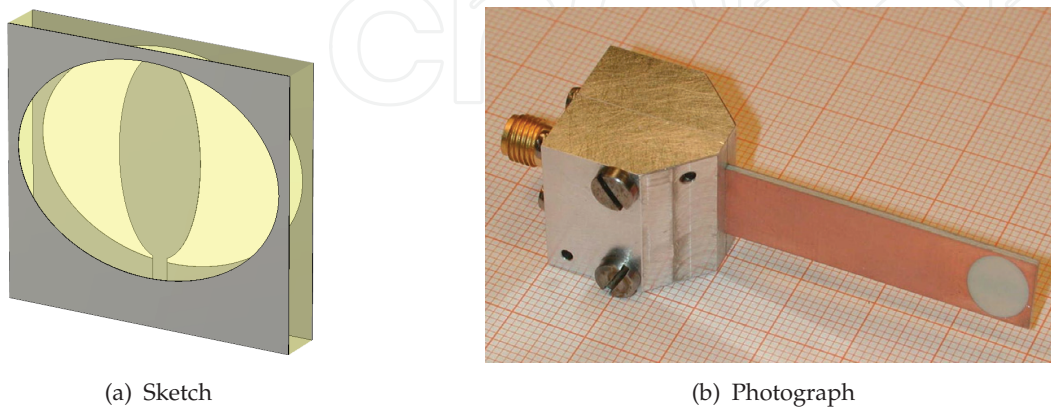
Figure 4. Sketch of the tissue optimized antenna and photograph including microstrip-to-coaxial transition.

In order to connect the antenna to a coaxial cable, a broadband transition from the triplate line to a coaxial line is applied [19]. The realized antenna including this transition is depicted in Fig. 4(b). The characterization of the tissue optimized antenna is performed in a tank filled with tissue-mimicking liquid approximating the permittivity and loss behavior of skin tissue. The chosen liquid is a 50% sugar solution in water [20]. Fig. 5(a) shows the return loss of the antenna being inside the sugar-water solution and compares its performance with a measurement, where the antenna is placed on both sides on human skin. Both measurement results agree very well and show a return loss of more than 10 dB above 3.8 GHz.

The radiation pattern is also measured in the tissue-mimicking liquid using two identical antennas and applying the two-antenna method. The obtained radiation pattern for the H-plane is presented in Fig. 5(b). There, the losses of the tissue-mimicking medium are compensated. Since the losses are increasing significantly with increasing frequency, measurements only up to 9 GHz are possible limited by the dynamic range of the measurement setup. Within this frequency range, a desired uniform and broad characteristic is achieved. Hence, UWB performance for a sufficiently small antenna for implants is demonstrated. For catheter localization additional miniaturization is required. A possible approach as well as more details about all presented antennas in Sec. 2.1 can be found in [20].

2.2. Transmitter MMICs

All integrated circuits reported in this section were realized in an inexpensive Si/SiGe HBT technology offered by Telefunken Semiconductors GmbH. Two kinds of transistors, with high f_T ($f_T = 80$ GHz, $BV_{CEO} = 2.4$ V) and with high breakdown voltage ($f_T = 50$ GHz, $BV_{CEO} = 4.3$ V) are available simultaneously. The process incorporates 4 types of resistors, MIM capacitors, as well as 3 metalization layers. All the devices were fabricated on a low resistivity 20Ω cm

(a) Reflection coefficient

(b) Measured radiation pattern in dB (H-plane)
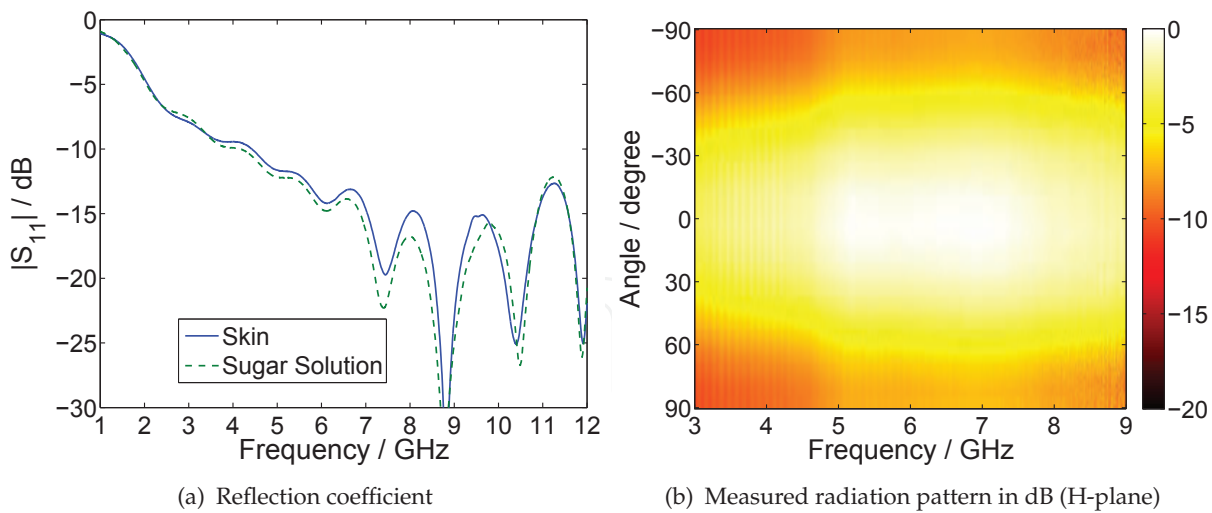
Figure 5. Reflection and radiation performance of the tissue optimized antenna.

substrate. The technology is fully adequate for impulse-radio-ultra-wideband (IR-UWB) applications.

Generating short time-domain impulses making efficient use of the spectral mask is the key challenge in IR-UWB systems. Approaches include the up-conversion of base band pulses to the allocated UWB frequency band using an oscillator and mixer [39] and direct generation based on damped relaxation oscillator [8]. Here impulse generators based on a quenched-oscillator concept with great circuit simplicity are presented. A cross-coupled LC oscillator is chosen as the core to introduce tunability of the waveform and the inherent convenience of achieving biphase modulation.

(a) Circuit schematic
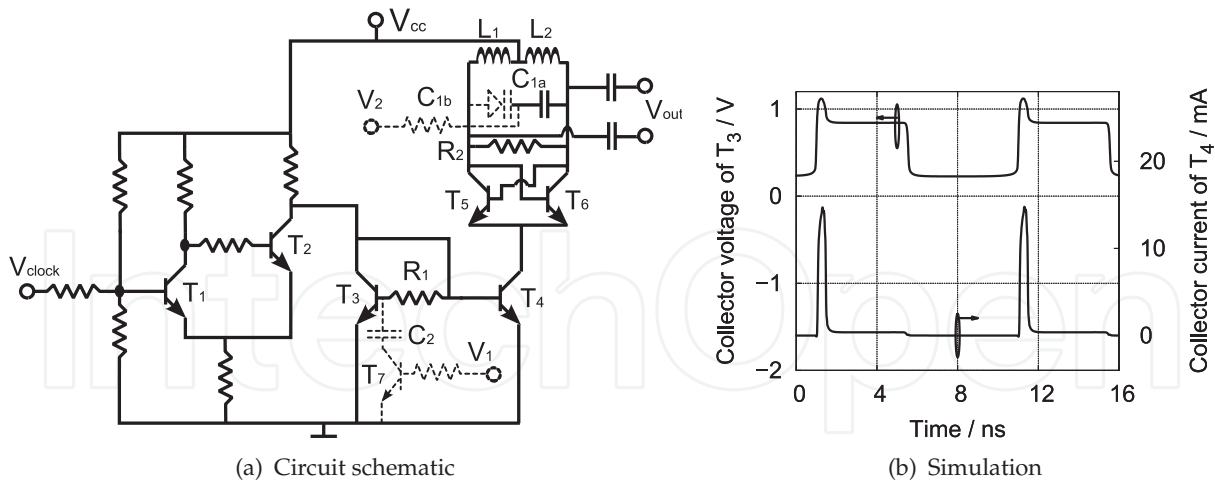
(b) Simulation

Figure 6. Complete circuit schematic of the UWB impulse generator. The dashed components (C_{1b}, C_2 and T_7) show the extension for tunability of the impulse shape for different spectral masks and transistor level simulation: the collector potential of T_3 and the collector current of T_4.

Fig. 6(a) shows the impulse generator circuit. First, disregard the components with a dashed line, which are the extention for tunability of the impulse shape. T_1 and T_2 form a Schmitt trigger, creating a fast rising edge at the collector of T_2 when a positive input signal triggers T_1 to be on. This reduces the effect of the time-domain influence of the input clock signal

on the output impulses. After an initial sharp increase, the collector potential of T_2 is pulled down again to a lower constant value by the current mirror formed by T_3 and T_4. So the collector potential of T_3 has a spike performance before it becomes stable, as shown in Fig. 6(b), which correspondingly generates a collector current spike at T_4, creating the envelope of the output impulse. During the rest of the period, the collector current of T_4 is too low to turn the oscillator on since T_3 is chosen much larger than T_4. The width of the current spike is determined predominately by the time constant τ of the charging circuit including the resistor R_1 and the base-emitter capacitor C_{be3} of T_3. τ can be written as

$$\tau = R_1 C_{be3}. \tag{1}$$

The amplitude of the current spike can be easily adjusted by changing the size of T_4. The repetition rate of the current spike train is equal to the input signal frequency and limited by the spike width.

The LC oscillator is activated by the current spikes once the collector currents of the cross-coupled pair (T_5 and T_6) are high enough to create a negative real part of the impedance. A slight asymmetry in the cross-coupled pair ensures that the oscillation always starts with the same phase and shortens the start-up time which in turn reduces power consumption because the necessary current spike width for a given output impulse envelope is shortened. R_2 is placed to quench the oscillator off more quickly immediately after the current spikes have disappeared. Thus, short-time domain impulses with a repetition rate equal to the input signal frequency are generated. The center frequency ω_0 of the oscillation is mainly determined by L_1, L_2, C_{1a} and the parasitic capacitance from the cross-coupled pair C_{para}. ω_0 can be expressed as

$$\omega_0 = \frac{1}{\sqrt{(C_{1a} + C_{para})(L_1 + L_2)}}. \tag{2}$$

It is designed to be around 6 GHz to fit the FCC spectral mask. The microphotograph of this realized impulse generator is shown in Fig. 7(a). It is a quite compact design with an area of 0.50 x 0.60 mm^2 due to a simple circuit topology.

(a)   (b)
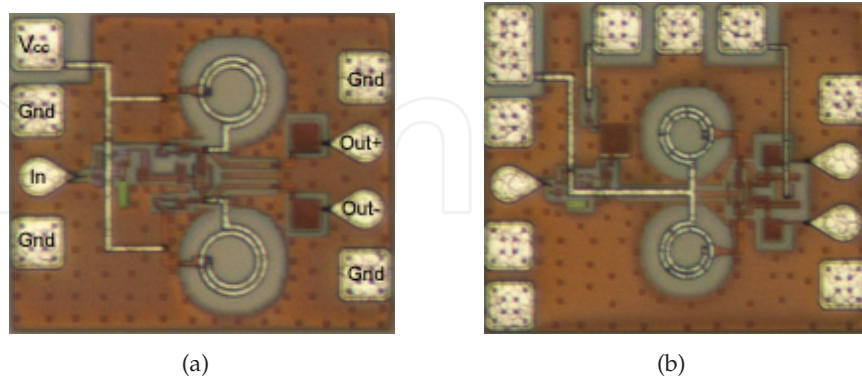
Figure 7. Microphotographs of (a) the realized UWB impulse generator shown in Fig. 6(a) excluding the components with a dashed outline and (b) the impulse generator tunable to FCC, ECC and Japanese spectral masks.

The impulses measured on-chip in time domain are shown in Fig. 8(a). The impulse generator is fed with a 100 MHz and 1.3 GHz sinusoidal signal separately. The differential signal is

(a) Time domain   (b) Spectrum
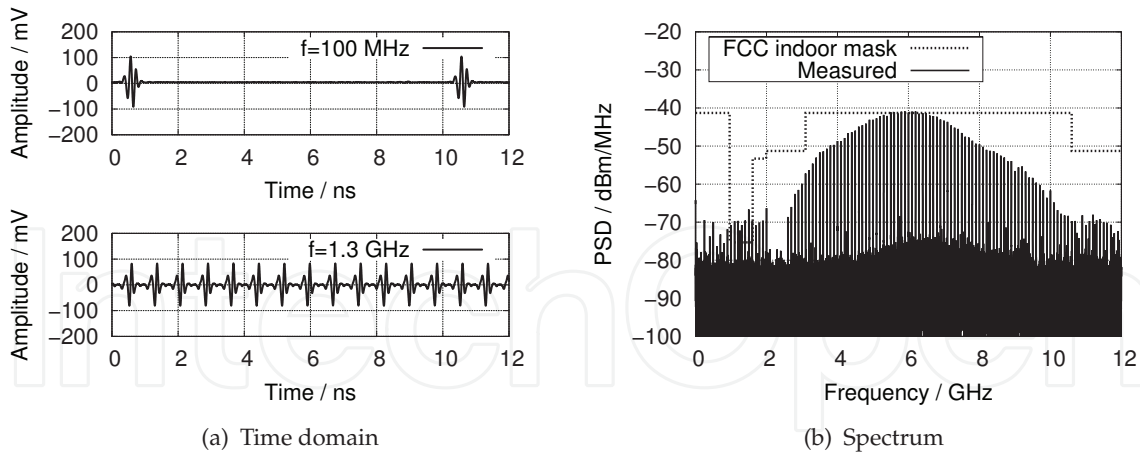
Figure 8. Measured results of time-domain output impulse waveforms at 100 MHz and 1.3 GHz repetition rate and the spectrum of the 100 MHz impulse train, demonstrating compliance with the FCC indoor spectral mask. The impulse generator is shown in Fig. 7(a)

displayed using the subtraction feature of a real time oscilloscope. The measured results show a peak-peak amplitude of 200 mV, and a full width at half maximum (FWHM) of the envelope of 0.3 ns. This circuit has a very low power consumption: 6 mW at 100 MHz and 10 mW at 1.3 GHz. The spectrum of the measured 100 MHz impulse train can be seen in Fig. 8(b). The maximum power spectral density (PSD) is -41.3 dBm per spectral line, and it has a 10 dB bandwith of 4.9 GHz from 3.5-8.4 GHz. It shows that the output spectrum complies well with the FCC mask for indoor UWB applications.

The two parameters (τ and ω_0) which determine the impulse parameters (envelope and osillation frequency) are easily modified. This is shown by the dashed components in Fig. 6(a). C_2 and T_7 are introduced to modify the envelope by changing the capacitance between the base of T_3 and ground, switching C_2 in and out. When $V_1 = 0$, T_7 is off, τ is the same as before, resulting the emitted impulses to conform to the FCC mask. When $V_1 = 1$ V, T_7 is on, the charging circuit will include R_1 and C_{be3} in parallel with C_2. In this case, the time constant τ_1 can be written as

$$\tau_1 = R_1(C_{be3} + C_2). \qquad (3)$$

Since C_2 is chosen much larger than C_{be3}, the envelope width of the impulses is larger in this situation, suiting for ECC or Japanese masks depending on the center frequency adjustment. The tank circuit capacitance is now formed by C_{1a} in series with a varactor C_{1b}. The oscillation frequency can be expressed as

$$\omega_0 = \frac{1}{\sqrt{(\frac{C_{1a}C_{1b}}{C_{1a}+C_{1b}} + C_{para})(L_1 + L_2)}}. \qquad (4)$$

Through changing the varactor capacitance C_{1b} with V_2, the center frequency ω_0 is adjustable. Depending on the applied voltages V_1 and V_2, the generated impulses conform to the FCC, ECC mask, or Japanese mask. The microphotograph of this tunable impulse generator can be seen in Fig. 7(b). It is quite compact with an area of 0.53 x 0.61 mm^2.

By setting $V_1 = 0$ and $V_2 = 2$ V, the LC oscillator is triggered with a shorter current spike. So the generated waveform is similar as shown in Fig. 8(a), targeting the FCC mask. This impulse

generator is suitable for the ECC mask when $V_1 = 1$ V and $V_2 = 2.3$ V. Under these conditions, the LC oscillator is triggered by a longer current spike with a FWHM of 2 ns. The measured output impulse train can be seen in Fig. 9(a). The impulses have a peak-peak amplitude of

(a) Time domain   (b) Spectrum
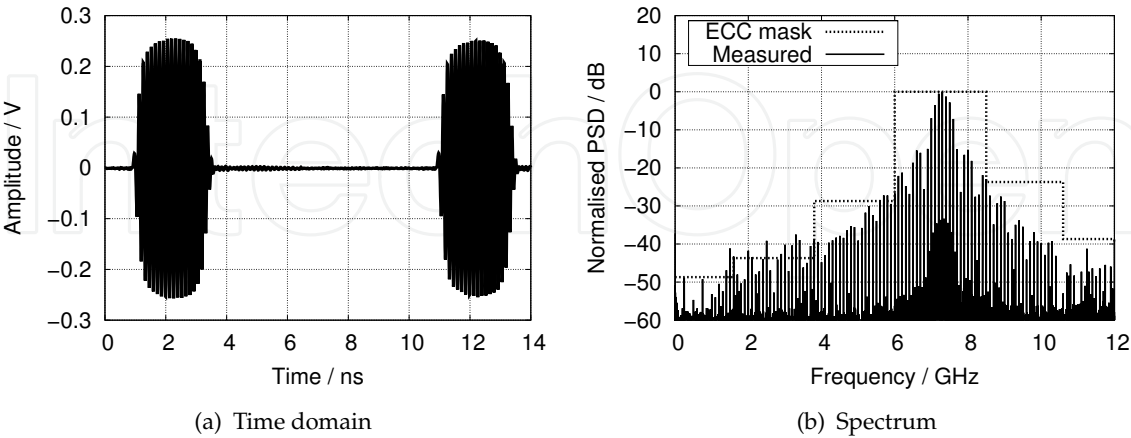
Figure 9. Measured results of impulse waveform in time domain and normalized PSD of the tunable impulse generator output signal setting for compliance with the ECC UWB mask.

0.5 V. The circuit has a total power consumption of 10 mW and a maximum output impulse repetition rate exceeding 300 MHz in this case. The normalized PSD of the impulse train has a center frequency around 7 GHz with a 10 dB bandwidth of 600 MHz, shown in Fig. 9(b). It fits well into the ECC mask. By changing the value of V_2, the center frequency of the impulses will be shifted, this makes the circuit usable for the Japanese mask. The measured output signal

(a) Time domain   (b) Spectrum
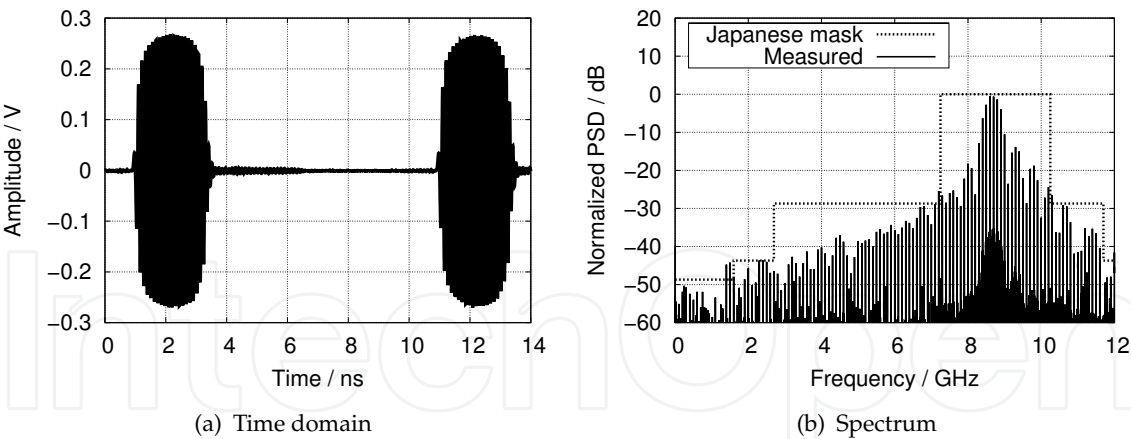
**Figure 10.** Measured results of time domain waveform and normalized PSD of the output signal targeting the Japanese UWB mask.

in the time domain with $V_{tune2} = 6$ V is shown in Fig. 10(a). The measured impulse train has a similar envelope as the mode targeting the ECC mask because the triggered current spike has the same width. The peak-peak amplitude of the impulses whose envelope has a FWHM of 2 ns is 0.5 V. The complete power consumption in this mode is 10 mW. The spectrum is presented in Fig. 10(b). It shows that the center frequency is shifted to 8.7 GHz for a good fit to the Japanese mask.

The performance under these three modes is summarized in Tab. 1. This impulse generator can be used for on-off keying (OOK) and pulse-position modulation (PPM) in all these three modes.

Mode (setting)	10dB bandwidth (GHz)	V_{PP} (V)	power cons. (mW)
FCC $V_1=0$, $V_2=2.0$ V	4.2	0.36	6
ECC $V_1=1$ V, $V_2=2.3$ V	0.6	0.5	10
Japanese mask $V_1=1$ V, $V_2=6$ V	0.6	0.5	10

**Table 1.** Performance summary of the tunable impulse generator.

Biphase modulation capability can be introduced by modifying the DC currents flowing in the individual branches of the differential LC oscillator. As shown in Fig. 11(a), additional branch currents are set through current mirrors T_7, T_9 and T_8, T_{10}. When the input data signal is

(a) Circuit schematic   (b) Microphotograph
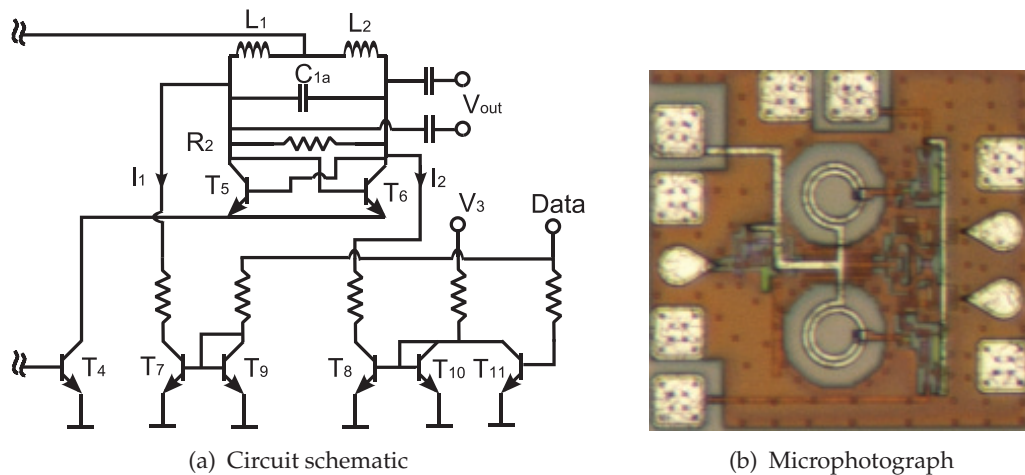
Figure 11. Adding biphase capability to the impulse generator in Fig. 6 and the microphotograph of the impulse generator with biphase modulation function.

low, transistor T_9 is off, and the collector current I_1 of T_7 is zero because of the current mirror configuration to T_9. Meanwhile, the applied voltage V_3 will generate a collector current I_2 in T_8 through the current mirror configuration of T_8 and T_{10}, because T_{11} is off. When the data signal is high, T_{10} switches into saturation and T_8 blocks, which causes I_2 to be zero. At the same time, the high potential at the base of T_9 introduces a collector current I_1 in T_7. Thus, oscillation will start in one of these two phase states once the tail transistor T_4 is turned on, constituting the biphase modulation. Additionally, this asymmetry shortens the start-up time, which in turn reduces the power consumption. The fabricated IC is shown in Fig. 11(b). It has an area of 0.56 X 0.53 mm^2.

The measured time domain waveforms with different voltage potentials applied to the data port can be seen in Fig. 12(a). The results show a peak-peak amplitude of 260 mV and an envelope width of 0.3 ns FWHM. The orientation of the impulses is clearly reversed, showing a perfect biphase modulation. Fig. 12(b) shows the spectrum of a 200 MHz impulse train with the data port connected to ground. It is centered around 6 GHz with a 10 dB bandwidth of
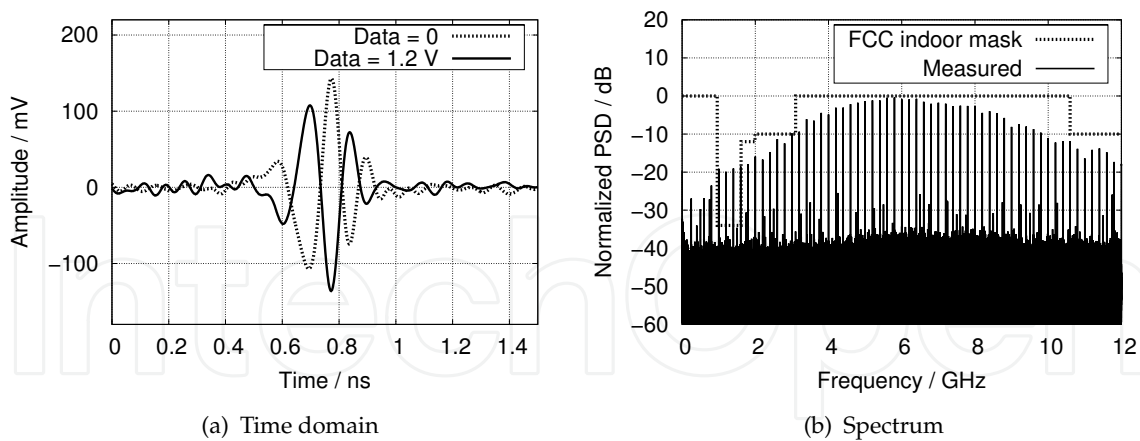
Figure 12. Measured time-domain results of biphase modulated impulses with different applied voltages at the data port and the spectrum information of a 200 MHz impulse train with the data port connected to ground.

6.7 GHz from 3.1 - 9.8 GHz, which complies well with the FCC spectral mask for indoor UWB systems.

2.3. Receiver MMICs

Two different types of receivers will be described in this section. Energy detection receivers are implemented for on-off keying (OOK) communications and localization applications, they are conceptually simple and do not require syncronization, but are also sensitive to interference. Correlation detection receivers are introduced to solve this problem, they are more robust to interference, but require accurate timing synchronization with the transmitter. This problem is eliminated in radar applications, because transmitter and receiver are co-located and synchronized with a common reference.
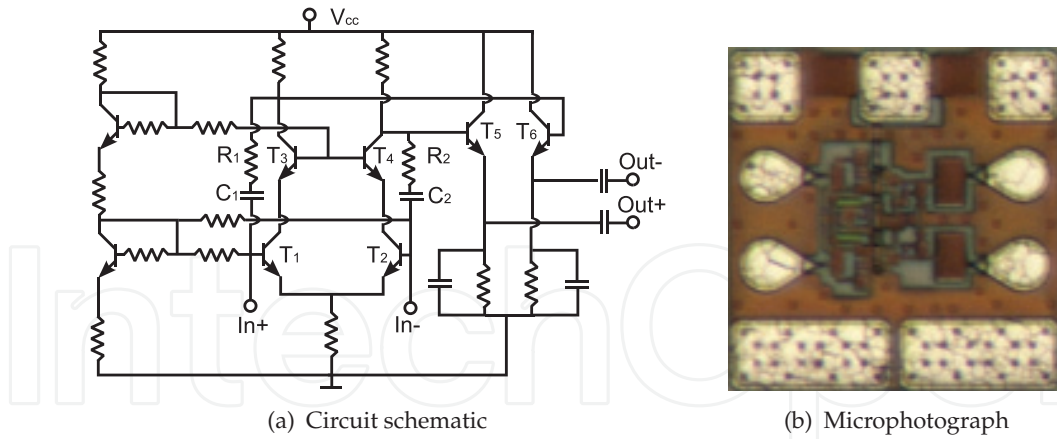
A fully differential UWB low-noise amplifier is a key element for both receivers. The LNA should provide a low noise figure, a high gain, a flat frequency response, and a small group delay variation within the complete frequency range. Another key component is a four quadrant analog multiplier, which performs the squaring operation in the energy detection receiver and the multiplication operation in the correlation receiver. Detailed explanation of these components will be described below.

2.3.1. Fully differential UWB low-noise amplifier

Fig. 13(a) shows the fully differential UWB low-noise amplifier schematic. It consists of a differential cascode, followed by two emitter follower stages as buffers. Input and output are differential as the LNA will be connected to a symmetrical antenna, and shall feed a Gilbert cell type analog multiplier directly, without an unbal circuit. The symmetry of the emitter-coupled pair is achieved by placing identical transistors and passive components in the two branches.

T_1 through T_4 form the differential cascode which is biased by the stacked current mirror. The primary reason of the cascode configuration is to reduce the Miller effect at the input port, increasing the bandwidth. The shunt-shunt feedback (R_1, C_1 and R_2, C_2) further broadens

(a) Circuit schematic

(b) Microphotograph

Figure 13. Complete circuit schematic and the chip microphotograph of the fully differential low-noise amplifier.

the bandwidth and improves the input matching simultaneously. Careful selection of input transistor size and adjusting the bias point was done as a compromise between optimum current density for minimum noise figure, noise-matched input impedance and achievable bandwidth. The emitter size of T_1 is chosen to be 0.5 μm x 24.7 μm and the emitter current is 5 mA. The wide band noise and input power match were accomplished by the selection of input transistor with suitable biasing and shunt-shunt resistive feedback. A negligible penalty, with a maximum value of 0.2 dB, is achieved within the entire band for not achieving noise match exactly. T_5, T_6 form a differential emitter follower buffer. The emitter degeneration capacitors are used to improve the buffer bandwidth.

The microphotograph of this differential LNA is shown in Fig. 13(b). Because this design is completely inductor-less, the IC has an extremely small size of 0.37 X 0.38 mm^2 including all bound pads. The lowest available metal layer was placed below the large-sized bonding pads to provide a ground shield, as otherwise the noise figure may be deteriorated by the substrate noise pick-up.


(a) S-parameters
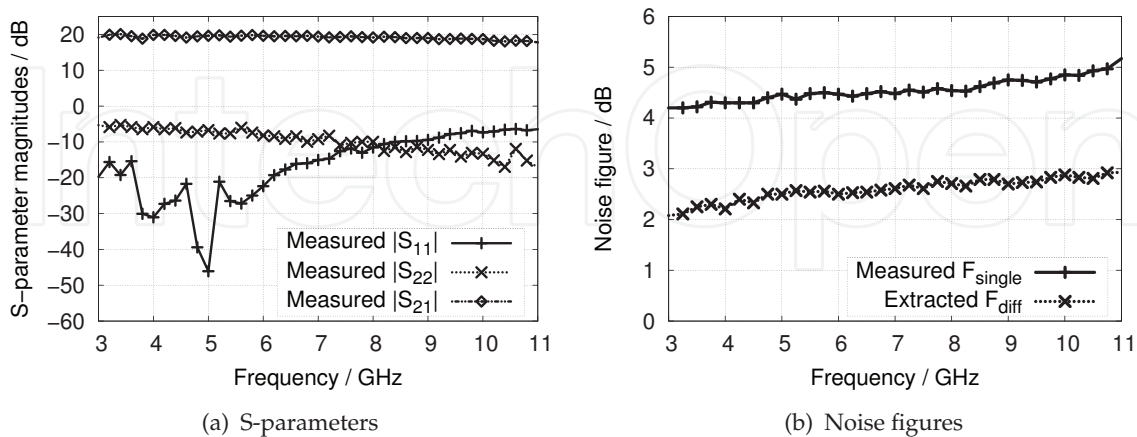
(b) Noise figures

Figure 14. Measurement results of the S-parameter magnitudes and single-ended and extracted differential noise figures.

One drawback of the differential configuration is a complex measurement setup. Two identical passive microstrip line UWB baluns are used for differential S-parameter

measurement. The influence of the baluns is removed during the calibration process. The measurement is restricted to 3 - 11 GHz due to the operating range of the UWB baluns. Fig. 14(a) shows the measured S-parameters. The non-ideal performance of the UWB baluns introduces ripples in the measured curves. The measurement results show a differential gain of 19.9 dB with a 1.8 dB variation, the input matching has a value of smaller than -7 dB and the output one is smaller than -6 dB in the complete FCC allocated frequency range. The method in [2] is adopted to extract the differential noise figure. First a single-ended noise figure F_{single} is measured from port In+ to Out- with the other ports terminated by 50 Ω resistors. Then, by measuring the transducer gain from port In+ to Out- (G_{31}) and Out+ to In+ (G_{32}), the differential noise figure can be extracted as

$$F_{diff} = 1 + \frac{1}{G_{31} + G_{32}}(F_{single}G_{31} - G_{31} - G_{32}). \tag{5}$$

Fig. 14(b) shows the information of the noise figures. The differential noise figure varies from 2 dB at 3 GHz to 2.9 dB at 10.6 GHz. Small group delay variation within the entire band is required for single-band IR-UWB systems. As depicted in Fig. 15(a), the group delay variation is smaller than 15 ps within the complete band. Fig. 15(b) shows the measured large signal behavior at 7 GHz of this differential amplifier. The input 1 dB compression point is -17.5 dBm. The complete power consumption of this differential LNA is 77 mW.

(a) Group delay

(b) Gain
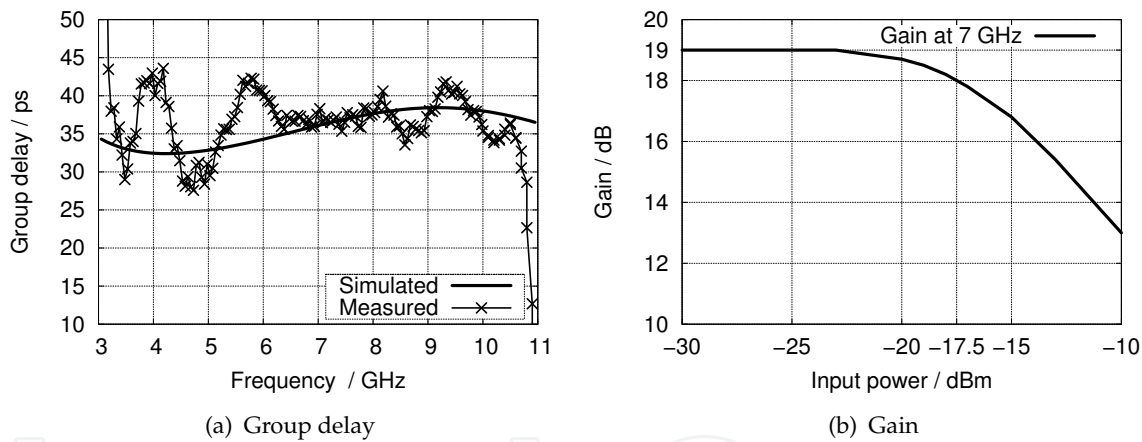
Figure 15. Measured results of group delay versus frequency and gain depending on the input power.

2.3.2. Energy detection receiver

The core of energy detection receivers is a squaring circuit. Fig. 16(a) displays the squaring circuit based on a Gilbert cell four quadrant multiplier comprising two differential stages in parallel with cross-coupled output, complemented by a low-pass filter and a differential output buffer. The squaring operation is realized by connecting the same signal to both inputs of the Gilbert cell. The signal fed to the lower pair of the Gilbert cell is taken directly from the LNA output transistors, while the signal fed to the top quad is passed first through the emitter follower buffer. Both paths introduce almost the same group delay. Thus, the two branches of the input signal arrive simultaneously at the multiplier, ensuring an exact squaring operation. The load resistors (R_1, R_2) of the Gilbert cell, together with shunt capacitors (C_1, C_2) of the

(a) Circuit schematic   (b) Microphotograph
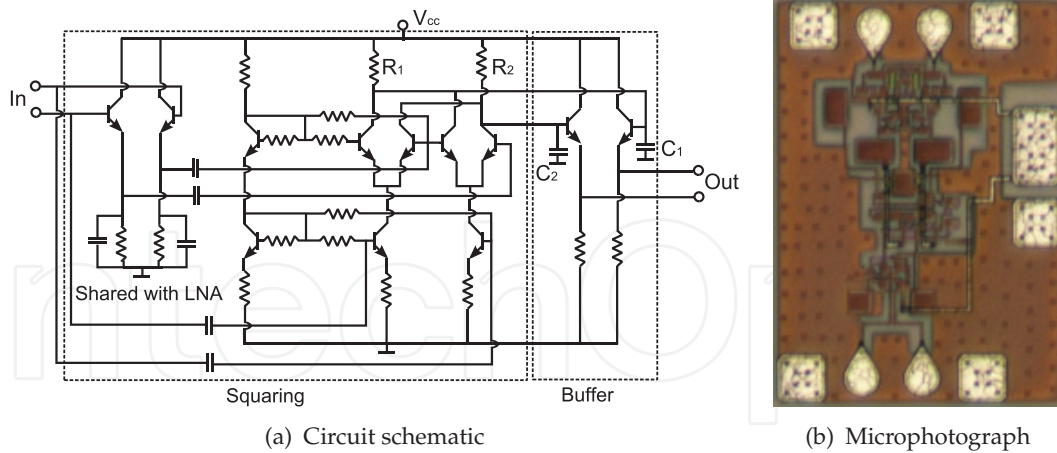
Figure 16. Squaring circuit, low-pass filter and buffer of the energy detection receiver.

output buffer form low-pass filters with 1 GHz 3 dB bandwidth, which are needed for the envelope detection. The LNA from Fig. 13(a) is added to complete the energy detection receiver, which totally consumes 108 mW. Fig. 16(b) shows the microphotograph of the fabricated receiver IC, it measures 0.43 mm x 0.61 mm, including bond pads.

For testing the energy detection receiver, a 700 Mbit/s return-to-zero (RZ) impulse train was generated by the impulse generator shown in Fig. 6(a), which has a power comsumption of 7.5 mW at this rate. The transmitter and receiver ICs are seperately mounted on Rogers RO4003C substrates which also carry the dipole-fed circular slot antennas discussed in 2.1.1, and are wire-bonded to microstrip transmission lines feeding the antennas. The two antennas are placed at a distance of 30 cm. Fig. 17(a) shows the input data sequence from a pattern

(a) Data sequence   (b) Output
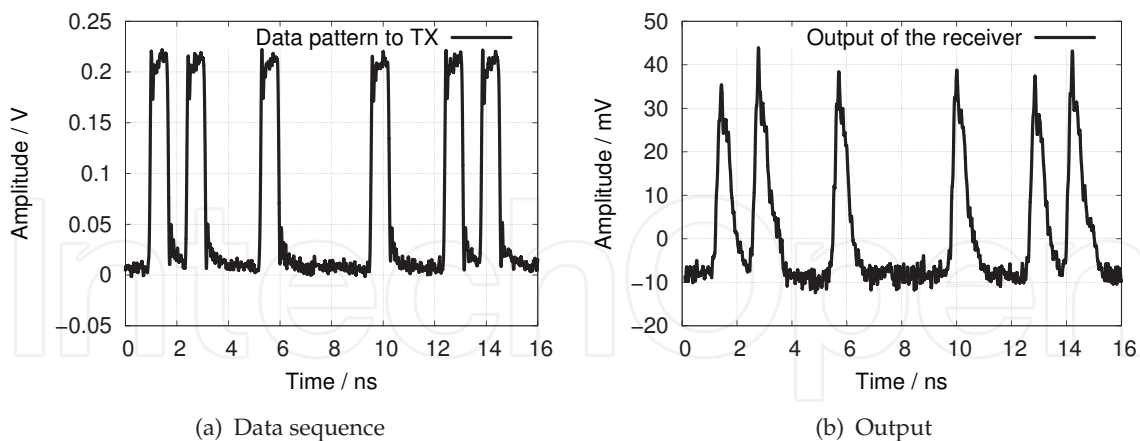
Figure 17. OOK transmission experiment at 700 Mbit/s over 30 cm, data sequence (700 Mbit/s data rate) applied to the transmitter and detected signal at the receiver output.

generator. The corresponding detected impulse envelopes with a peak amplitude of 40 mV at the output of the receiver IC can be seen in Fig. 17(b). This experiment clearly demonstrates that the simple transmitter/receiver combination can be used to transmit significant bit rates over short distances. Detailed measured results of the receiver are shown in [23].

2.3.3. Correlation detection receiver

Coherent detection receivers are based on the cross-correlation realized by feeding the received signal and the on-chip generated template impulse into a wideband analog four-quadrant multiplier and subsequent low-pass filtering. Fig. 18(a) shows the block diagram of the correlation receiver. The multiplier-based correlation is done in the RF domain, which leads to an energy efficient solution by omitting power-hungry wideband ADCs. In a radar setup, the transmit and receive clocks need to be phase adjusted, which in practice is done by a DDS board. The complete schematic of the UWB analog correlator circuit

(a) Diagram   (b) Circuit Schematic
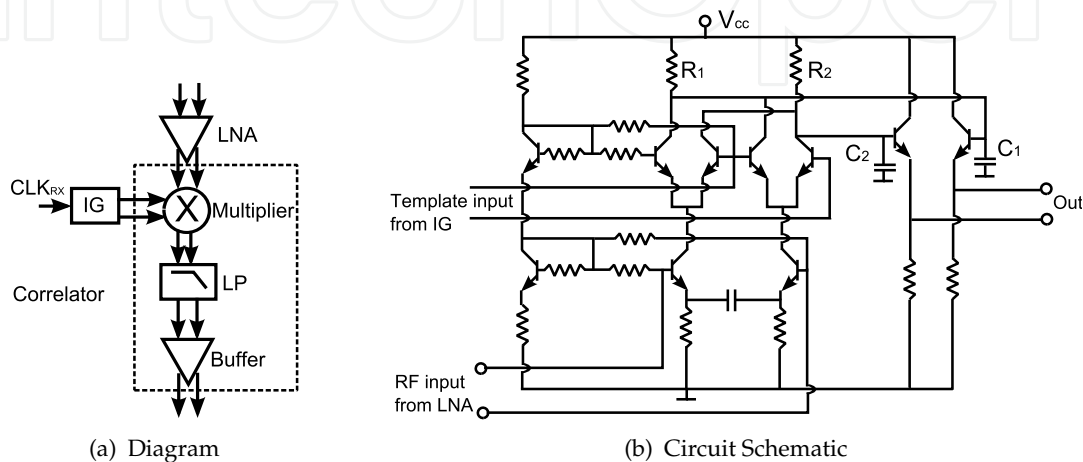
Figure 18. Architecture of the correlation receiver system and the schematic of the correlator with a true multiplier, a low-pass filter and a buffer.

can be seen in Fig. 18(b). The core of the correlator is again a Gilbert cell which acts as a wide-band multiplier with proper template impulse amplitude applied to the switching quad. Capacitively shunted resistive emitter degeneration results in the necessary gain flatness over the whole UWB frequency band. The low-pass filters are formed by the load resistors (R_1, R_2) of the Gilbert-cell with the shunt capacitors (C_1, C_2) of the buffer, the same as shown for the case of the energy detection above. The correlator consumes 35 mW.

The complete receiver IC, including the differential LNA, the correlator and the template impulse generator, is shown in Fig. 19(a). It measures $0.43 \times 0.61 \, \text{mm}^2$ and consumes a total DC power of 130 mW. To demonstrate the correlation performance of the receiver, the receiver IC was connected to a dipole-fed slot antenna, and placed at a distance of 20 cm from the transmitter. A small offset frequency of 100 Hz was introduced between the transmitter and receiver clocks, making the template impulses continuously sweep through the received signal. The measured cross-correlation can be seen in Fig. 19(b). More details of the correlation receiver can be found in [24].

2.4. Monostatic radar MMICs

All UWB radar sets reported so far use a bistatic antenna configuration. A monostatic UWB radar would significantly reduce the size of IR-UWB sensors because of the elimination of one antenna. However, implementation of rapid switching between the transmit and the receive path is difficult to realize in either this low-cost bipolar-only or CMOS technology. Here, a

(a) Microphotograph   (b) Correlation
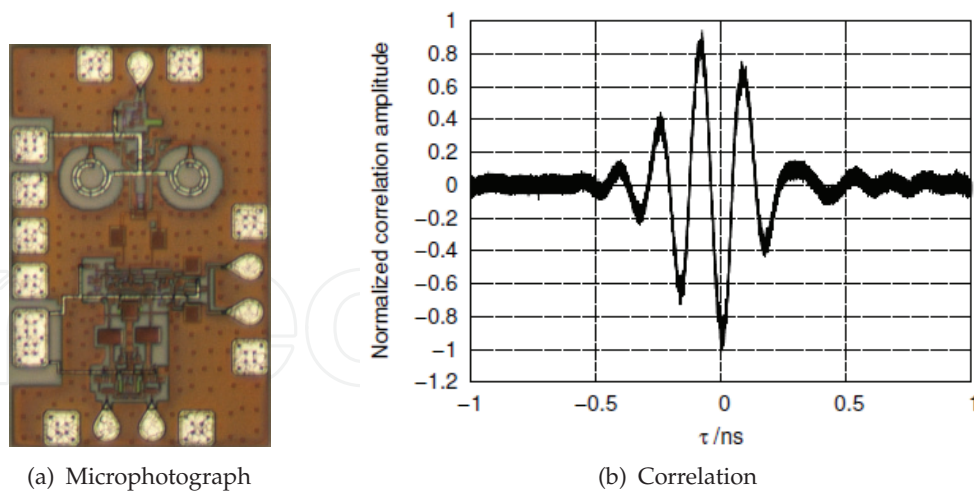
Figure 19. Chip micrograph of the fully integrated correlation receiver and the measured normalized cross-correlation of the received impulse with the template impulse.

novel front-end concept based on a merged impulse generator/low noise amplifier, shown in Fig. 20(a) is proposed. In this design, the input of the differential low-noise amplifier is tied

(a) Diagram   (b) Microphotogragh
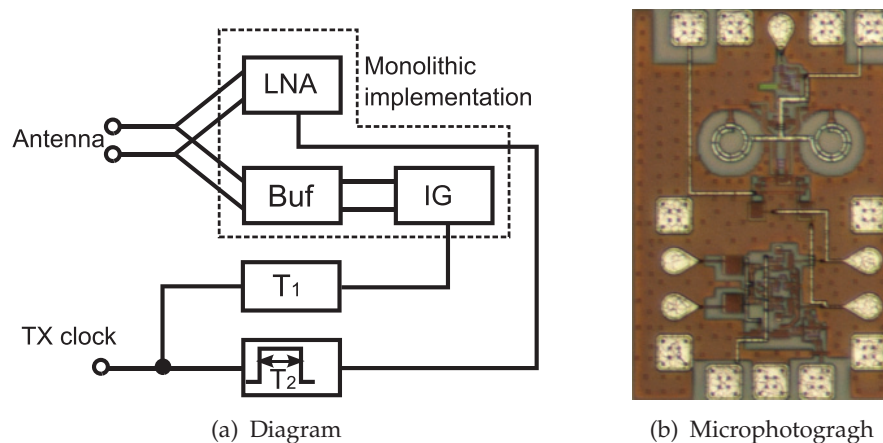
Figure 20. Block diagram and chip photo of the proposed monostatic UWB radar front-end.

together with the output of a buffer amplifier following the impulse generator. An external monoflop and a bandgap reference circuit ensure that the LNA is disabled during the impulse emission. The LNA bias is recovered after the impulse has been transmitted, and it returns to full gain within 1.5 ns. The added parasitics of the buffer are included in the design of LNA.

Fig. 20(b) shows the fabricated IC. In the experimental test, the antenna terminal is connected to two short coaxial cables, each of which feeds into a 10 dB attenuator shorted at the far end. An approximately 1 ns delay is generated by the coaxial cable and attenuator, corresponding to a distance of 30 cm in air. The measured time domain trace at the output of the differential LNA can be seen in Fig. 21. The significant common-mode transients due to the bias switching are completely invisible owing to the balanced setup. The result clearly shows the received impulse echo. Due to a high isolation of the 'cold' low-noise amplifier, the crosstalk from the transmitted pulse is barely visible and will not influence the further processing.
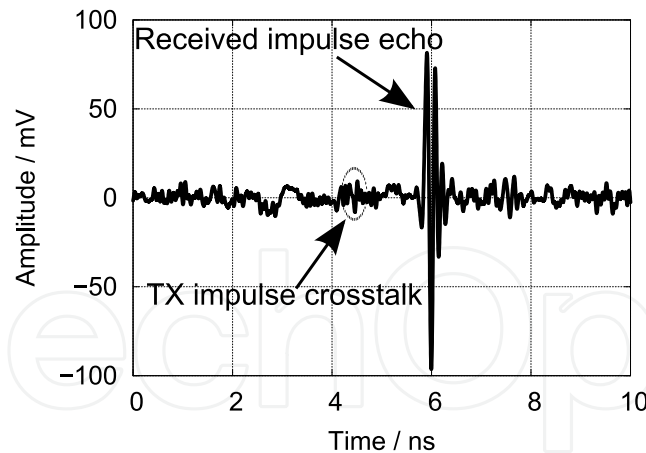
Figure 21. Real time oscilloscope trace showing the functional test of the monostatic radar frontend, displaying transmitted pulse crosstalk and received pulse echo.

3. Signal processing

3.1. Energy detection for UWB communications

For UWB communications, the detection of transmit symbols can be done with a coherent or a non-coherent method. Typically, with perfect synchronization, the coherent detection based on correlation gives a better performance than non-coherent detection. Coherent detection is known to be the optimum method with respect to the bit error rate (BER) for AWGN channels. In case of multipath propagation channels, the transmit impulse and the channel impulse response together (convolved) must be used for correlation detection, and in general more complex signal processing is required. Analog signal processing is considered here because analog to digital conversion for UWB signals is hardly available and requires high power consumption. Unfortunately, the coherent approaches are not well suited for our large bandwidth analog signal processing within the receiving frontend. Energy detection is usually preferred because, if applied in a proper way, no channel impulse response is needed in the receiver. Moreover, energy detection is also robust with respect to synchronization accuracy. In its basic form the energy detector consists of a squaring device, an integrator, a sampler and a decision device.

Pulse position modulation (PPM) and On-off keying (OOK) are modulation techniques that are typically used in combination with energy detection. The data modulation is performed by changing the position or amplitude for PPM and OOK respectively. The detection of PPM is easier to perform since comparing the signal energy at two different intervals is enough, while OOK requires threshold estimation. We look at the BER performance of PPM with respect to synchronization and multipath propagation. Different levels of synchronization in AWGN channels (perfect, ± 20 ps, and ± 40 ps) and a perfect synchronization for a multipath channel are considered. The errors in the synchronization accuracy are uniformly distributed. The transmitted signal is an impulse train of fifth derivative Gaussian functions ($\sigma = 51$ ps) with PPM modulation. The tested channels AWGN channel and a multipath channel with delay spread are assumed to be shorter than 4 ns, which is half of the impulse repetition interval. The correlation receiver uses a template impulse (fifth derivative Gaussian) for correlation, and the correlation is centered at the first strongest path of the channel. The BER for all settings is shown in Fig. 22.
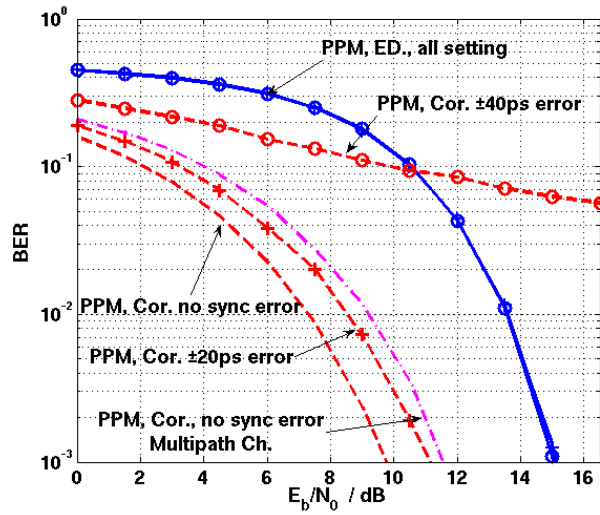
Figure 22. BER performance of PPM modulation for correlator and energy detection with AWGN channel and multipath channel.

The performance of the correlation receiver suffers from synchronization uncertainty and multipath propagation. This is due to the fact that the impulse used in UWB systems is very narrow and the impulse correlation receiver cannot capture all of the signal energy. On the other hand, the energy detector shows good performance also for non-perfect synchronization and multipath channel. We can conclude from the results that, with a performance trade-off, the energy detection is much more robust. Other challenges for implementing energy detection are multiuser capability and interference cancellation. These problems can be solved by the comb filter receiver presented in the following part.

3.2. Comb filter

The received signal power for medical applications are expected to be very small due to high attenuation in human tissue. We propose a receiver based on a comb filter to improve Signal-to-Noise ratio (SNR) before further processing. The comb filter is a feedback loop with an analogue delay and a constant loop gain of one for all frequencies. It is used to perform a coherent combination of the incoming UWB impulses. The feedback loop sums up the number of impulses used for the transmission of a data symbol/measurement and is reset after this. The coherent combination results in SNR improvement, interference suppression which come from different transmitters in a multiuser environment or narrowband interfering signals. Several UWB impulses are transmitted for one data symbol/measurement. One important feature of the concept is that the individual UWB impulses are weighted by +1 or -1 according to a spreading sequence. The UWB transmit signal $s(t)$ can be written as

$$s(t) = \sum_{k=-\infty}^{\infty} \sum_{n=0}^{N-1} c_n p(t - nT_c - kT_s), \tag{6}$$

where $p(t)$ is a UWB impulse and c_n is the spreading sequence. T_c is the period between two UWB impulses or 'chip period' and $T_s = NT_c$ is symbol period for communications or measurement period for radar/localization application. For communication, assuming a binary transmission, the impulse train of each data symbol can be modulated in different

ways. We consider three modulations using the direct sequence spread spectrum technique based on OOK, PPM, Code shift keying (CSK) ,i.e. DS-OOK, DS-PPM and DS-CSK. For DS-OOK, transmitting a train of impulses represents the data '1', while no impulse signals means '0'. For DS-PPM, the two basic waveforms for a binary transmission are different by time shift. For DS-CSK, the two waveforms result from two different spreading sequences. A decision threshold is not required for DS-PPM and DS-CSK which is a big advantage compared to DS-OOK. The basic waveforms for different modulation techniques are illustrated in Fig. 23.
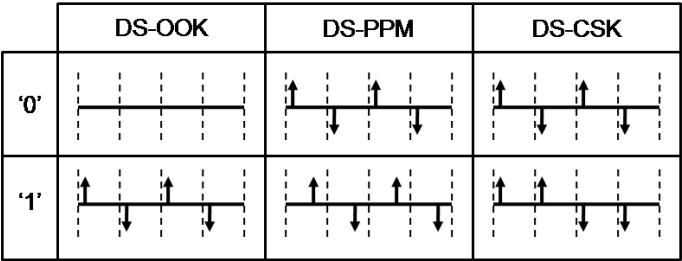
Figure 23. Comparison of UWB transmit signals for different modulation techniques.

Transmitted through the channel, the impulses are affected by the channel impulse response which is expected to be a multipath environment with or without a line-of-sight path. The chip period is chosen to be larger than the multipath spread, with the result that no interchip interference (i.e. no overlapping of channel impulse responses) occurs. We assume the channel to be time invariant within the symbol period. This means that the signal or basic waveform which represents one data symbol/measurement in the received signal consists of a corresponding number of channel impulse responses.

3.2.1. Basic comb filter receiver

The receiver based on the comb filter with remodulation is shown in Fig. 24. The receiver consists of an antenna, a LNA, a multiplier, the comb filter, the energy detector for communications and a correlator for radar/localization applications. This concept allows energy detection in a multipath and multi-sensor environment and amplification of the impulse response in the comb filter delay loop.

In the receiver, the received signal is multiplied with the spreading waveform (i.e. the sequence with rectangular "chips"). If the spreading sequence matches, the result is a periodically repeated channel impulse response with period T_c. After multiplication, the received impulses are delayed and summed up by the comb filter. At the output of the comb filter, only the last T_c period of every T_s is used for further processing which is expected to be an amplified and improved SNR channel impulse response. Interference from different UWB transmitters and other systems are eliminated at the comb filter. The process of remodulation and coherent combination at the comb filter is illustrated in Fig. 25.

Spreading is used not only for the multiuser or multi-sensor purpose, but also for shaping the power spectral density of the transmitted signal. The impulse train may have high spikes in the power density spectrum, because it has a periodic behavior over a longer time interval,
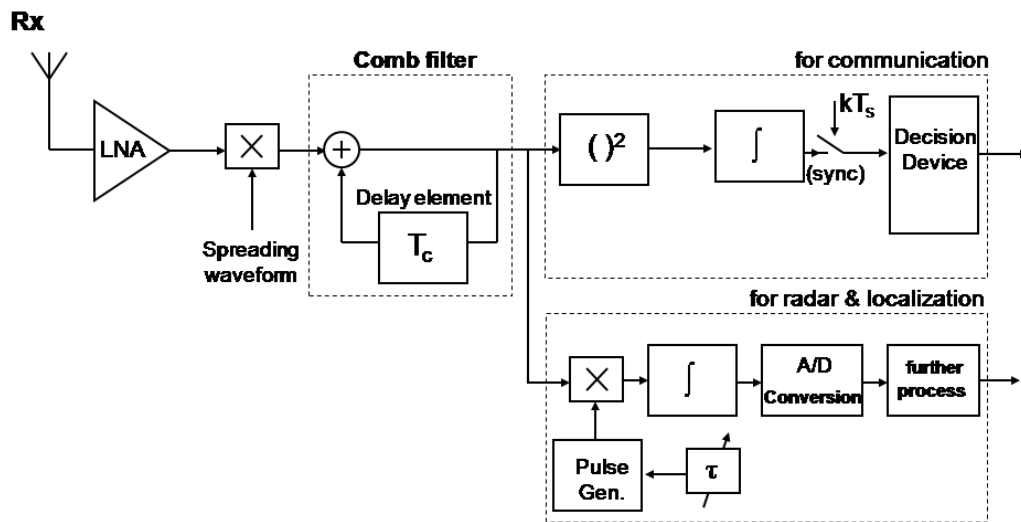
**Figure 24.** Block diagram of the basic comb filter based receiver.
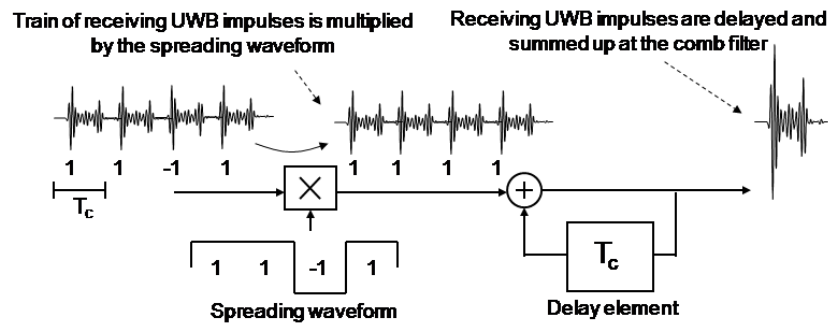
Figure 25. Comb filter principle in the receiver.

and hence it could violate the spectral mask requirement. The longer and more random the spreading sequence, the better. Of course, a direct restriction is given by the desired data rate.

3.2.2. Multiuser interference

In general we will have many transmitters or many sensors and different corresponding spreading sequences. The sequences are selected such that the mutual cross-correlation values are as small as possible. This guarantees that many transmitters can be used at the same time in the same area, e.g. several implants for digital transmission. The signals from all sensors are assumed to be transmitted in parallel with synchronization in a certain time window. The remodulation and the comb filter at the receiver is the crucial part in suppressing the multiuser interference (MUI). The weighting factors of the channel impulse response train after the multiplication are a scrambled version between transmit and receive sequence, if they are not the same. The accumulation at the comb filter would eliminate the MUI and the result of the weight is the cross-correlation values. The illustration of multiplication with the spreading sequence and comb filter accumulation of a signal with two different sequences is shown in Fig. 26.
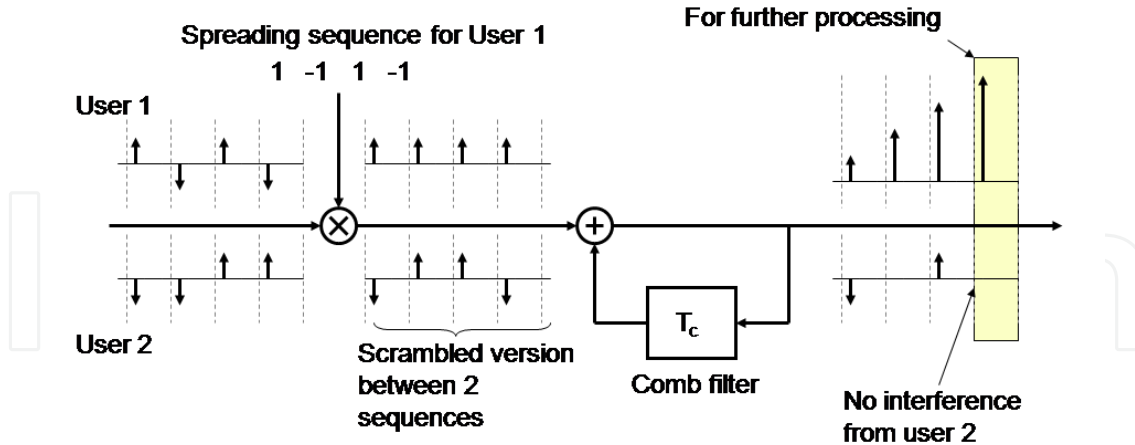
Figure 26. Illustration of multiuser interference suppression at the comb filter.

We assume synchronization in a certain time window between different users. With this assumption, we mainly consider m-sequences because they have low crosscorrelation and are simple to generate. Alternatively, binary zero-correlation-zone (ZCZ) sequence can also be considered. Unlike m-sequences, these sequences have a crosscorrelation of zero within a small window but the drawback is a smaller number of sequence in one set [40]. Binary ZCZ sequence sets were investigated in [37] for communication because of their potential to completely eliminate multi-sensor and interchip interference (ICI). A near-far problem was taken into account and we can see an advantage of this sequence set.

3.2.3. Signal-to-noise ratio improvement

The SNR of received signals can be significantly improved after the coherent combination in the comb filter, since the signal power grows quadratically, while the noise power grows only linearly. We first consider ideal components where there is no distortion in delay line and the comb filter has no loop gain. For the investigation of the SNR improvement, an AWGN channel is sufficient. A train of modulated UWB impulses and additive noise is the input signal to the multiplier. The SNR at the input of the multiplier is compared to the SNR after the comb filter to calculate the comb filter processing gain G_p. Fig. 27(a) shows an example of an input signal with a SNR = -15 dB (upper) compared to the output signal (lower). The SNR improvement can be seen clearly as the receiving impulse becomes visible after a few iterations. This comb filter signal processing results in a SNR improvement of $10 \log(N)$ dB, where N is the number of iterations. The UWB signal is algebraically added, therefore the signal energy is increased by a factor of N^2. On the other hand, the noise contributions in each chip are added in power, and therefore the noise energy within the symbol interval is increased only by a factor of N. For communications, the BER of PPM with correlation and energy detection also show the same improvement. The BER performance for DS-PPM with $N = 1$ and $N = 63$ using M sequence is shown in Fig. 27(b) . Using several chips per symbol with the comb filter approach gives a performance gain with respect to SNR but not to E_b/N_0 due to the difference in the data rate. For UWB transmission, the SNR cannot be improved by increasing the transmitted energy because of the spectral mask limitation. A trade-off between data rate and the SNR improvement at the receiving side has to be made.
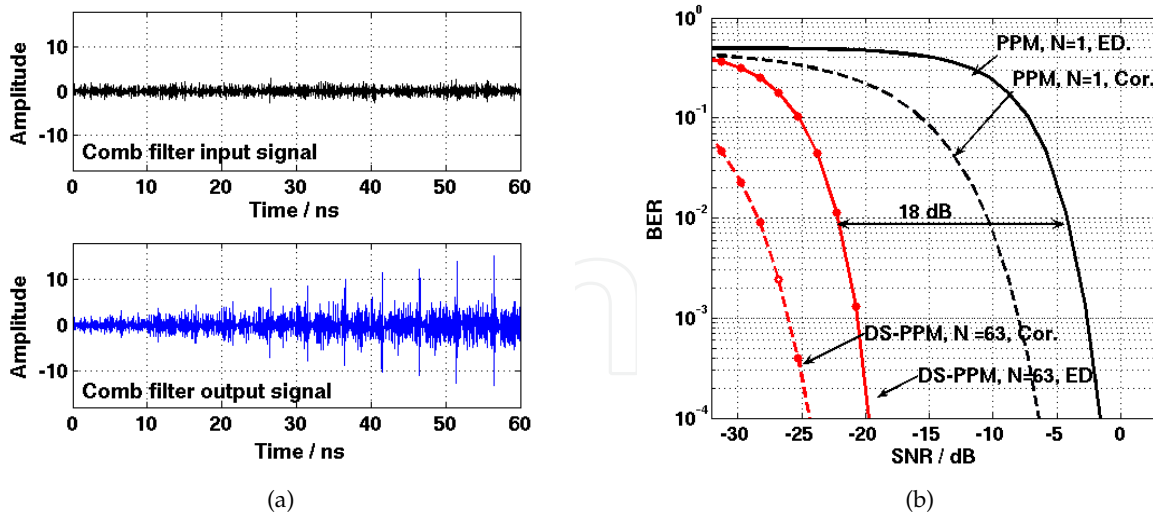
Figure 27. (a) Input and output of the comb filter with remodulation. (b) BER performance of DS-PPM
with N = 1, 63.

For physical systems this calculation is only valid if no instability is introduced. Therefore the
values of the gain G_c of the comb filter can only be in the range of 0-1, because otherwise an
oscillation occurs. G_c is designed to be one but considering real components, a loss in the loop
is possible. The comb filter processing gain G_p is a function of the gain G_c of the comb filter
and the number of iterations N. It can be calculated as

$$G_p = 10 \cdot \log_{10} \left(\frac{\left(\sum_{n=0}^{N-1} G_c^n \right)^2}{\sum_{n=0}^{N-1} G_c^{2n}} \right) \tag{7}$$

The maximum processing gain G_p of the comb filter is $10 \log(N)$ dB, when $G_c = 1$. The
processing gain is reduced if G_c is less than one. The relations between G_p, G_c and N are
shown in Fig. 28. We can see from Fig. 28(a) that the processing gain G_p saturated in the case
where G_c is less than one because the impulse energy vanishes after some iterations. With a
higher number of impulses per symbol, the comb filter loop gain has to be controlled more
precisely as shown in Fig. 28(b).

3.2.4. Narrowband interference

Since UWB covers a very large bandwidth, strong interference within the band is possible and
can cause problems at the receiver. Comb filter in combination with multiplication with the
spreading waveform can suppress narrowband interference very well. Only a periodic signal
that has a period which equals one or multiples of the comb filter delay can go through the
comb filter. The comb filter transfer function $H(f)$ is given as follows:

$$H(f) = \sum_{k=-\infty}^{\infty} T_s \cdot \text{sinc}(T_s(f - k/T_c)) \exp(-j\pi f T_s) \tag{8}$$

We can see that the transfer function of the comb filter consists of several peaks. The peaks
could be seen as tunnels that allow only signals with specific frequencies to pass. After the

(a)

(b)
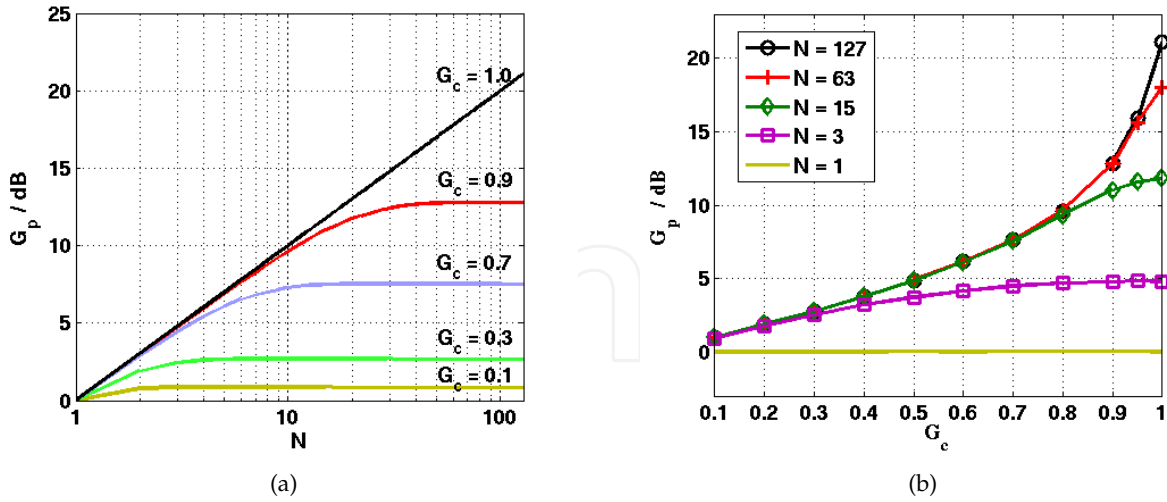
Figure 28. Relationship between processing gain G_p, comb filter loop gain G_c and impulses per symbol N.

multiplication with the spreading waveform in the receiver, the spectrum of the UWB signal has a shape matched to the transfer function of the comb filter (signal with period T_c). On the other hand, the narrowband interferer is spread by this multiplication and only some frequency components could go through the comb filter. The width of each peak depends on the number of chips per symbol. It gets smaller as the number of summation steps in the comb filter increases and as a result more interference is suppressed.

The improvement of the signal-to-interference ratio (SIR) is demonstrated in Fig. 29(a). The signals at the input of the comb filter are the UWB signal and a narrowband interference consisting of an IEEE 802.11a OFDM WLAN signal with a bandwidth of 16.66 MHz and a center frequency of 5.2 GHz. In this example, the input SIR of -15 dB is improved by 10 dB for $N = 63$. In addition, the BER performance of DS-OOK and DS-PPM in an AWGN channel with the same interference is shown in Fig. 29(b). The performance for both methods is improved with increasing number of chips per symbol. The degradation of the performance due to the narrowband interference for DS-PPM is much less than that for DS-OOK. The narrowband interferer gives a contribution to both integrator outputs for DS-PPM, and because the outputs are compared, the influence is reduced. For the DS-OOK the influence remains.
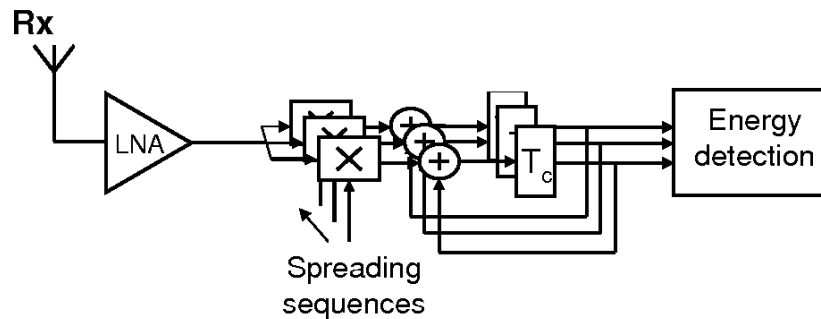
3.2.5. Shortened delay comb filter

The main challenge for implementing the comb filter based receiver is to realize the true wideband analog delay element. Shortening the delay means that overlapping channel impulse responses can occur at the receiver, the channel impulse response becomes longer than the chip interval T_c. As a result, after the comb filtering we get an amplified window-cut-out of the true impulse response with the window width T_c. It is shown in [35] that we can control the position of this window by adjusting the spreading sequence at the remodulation. The property of being able to extract different parts of the channel impulse response gives an opportunity to construct a receiver by using a rake concept. This means that for each part of the impulse response we have one rake branch where we calculate the energy. The modulation technique that is well-suited for this structure is DS-CSK. The block diagram
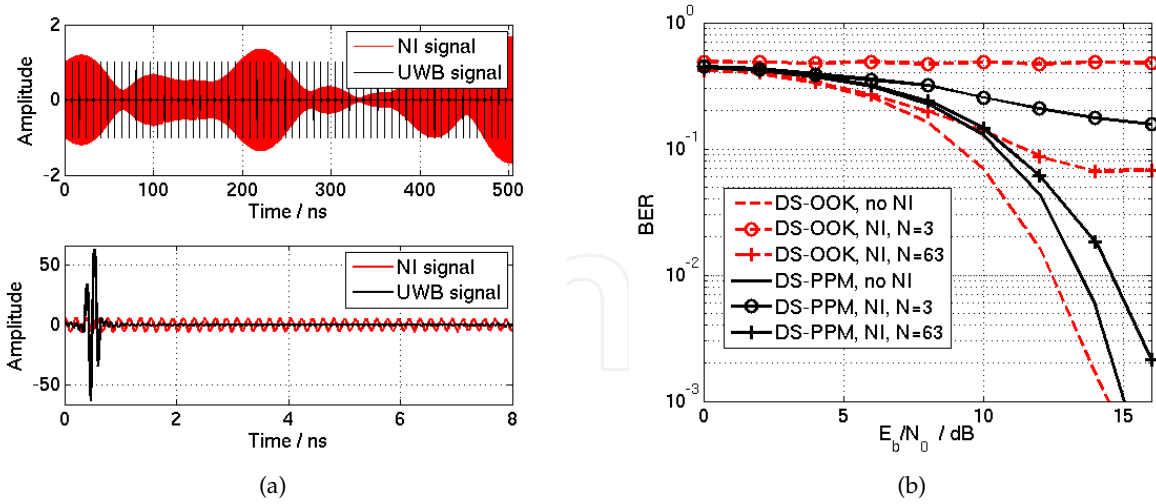
Figure 29. (a) Input and output of the comb filter with remodulation. (b) BER performance with SIR = -15 dB.

of the receiver for this concept is shown in Fig. 30. Note that the spreading sequences for the rake branches are cyclic-shifted versions of one single sequence. For DS-CSK, two parallel branches with different corresponding spreading sequence sets are needed. The results from two branches are then compared.

Figure 30. Block diagram of a rake-like comb filter receiver with energy detection.

In comparison to our basic concept described before, the delay is shorter. If the delay is shortened, for example, from 12 ns to 2 ns, this is much more realistic with regard to the realization. The performance of the new concept was verified by simulations. We used UWB impulses within a band from 4 GHz to 6 GHz. Note that this band is due to the Wireless Body Area Networks (WBANs) channel model we used [12] but it is not important for our concept, it could be any. The channel model consists of two groups of paths with a lognormal fading statistic for each group. We used 4000 channel realizations. The total propagation time of the channels is 12 ns. Eight users/sensors with the same average receive energy are considered. The spreading sequences were m-sequences with $N = 127$. The receive signal at the input of the comb filter is shown in the upper part of Fig. 31(a). Additive noise is not considered here to focus only on the ICI and MUI suppression. We can see that both, ICI and MUI are very strong here. The SIR in this example is -17 dB. In the lower part of Fig. 31(a) the original channel impulse response (black) is compared to the results taken from different rake branches (red). From the results we can see that the interference is suppressed very well.

We also look at the BER performance of this new concept in Fig. 31. A WBAN channel is used. For our original basic comb filter concept, $T_c = 12$ ns and 6 ns are considered. We label them as 'Basic 1' and 'Basic 2', respectively. For the rake-like receiver, we consider $T_c = 2$ ns with 6 rake branches which yield equivalent integration time of 12 ns. We can see that the performance of our original concept is getting worse if the delay is shortened. There is a loss of about 4 dB at the BER for 10^{-4}. The result for 'Rake-like' is comparable to 'Basic 1'. The results show that we can achieve a very similar performance to the original concept with much shorter analog delay elements.

(a)   (b)
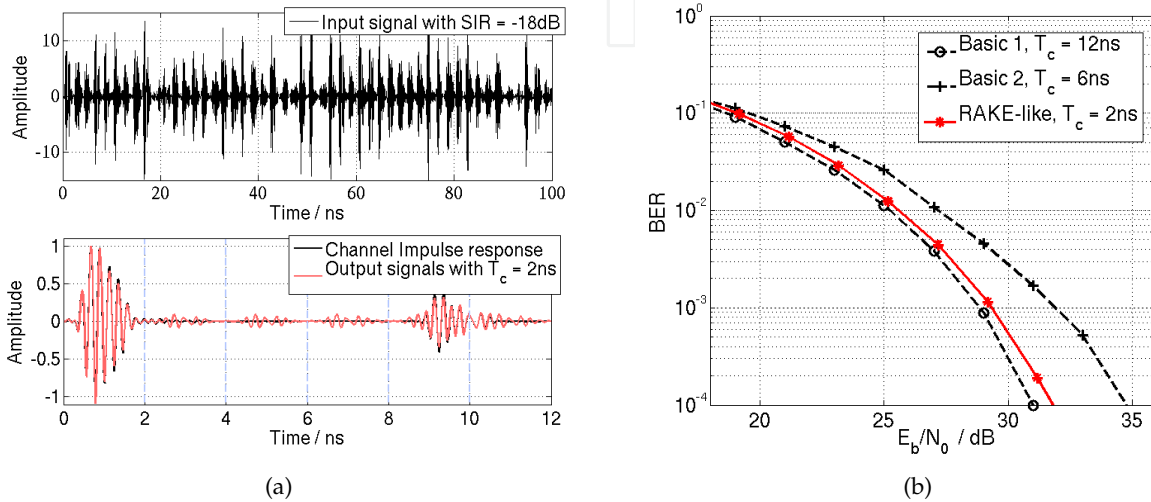
Figure 31. (a) Input signal of the comb filter (upper). Comparison between the actual channel impulse response and the output signal of the rake branches (lower). (b) Comparison of the bit error rate from different receivers.

3.3. Particle filtering

In this part we want to address an algorithm for movement tracking which can be used for radar and imaging application. The background is the application of IR-UWB for biomedical diagnostics, e.g. vital sign detection (like breathing/heart rate) and also tracking of body movements to compensate for errors which degrade the quality of inner body imaging. Simple methods such as tracking the maximum/minimum of the receive signal in a specific area perform reasonably well. A problem occurs if the peak of the signal cannot be easily identified. In cases with high attenuation, the estimation can become very bad for those simple methods. Another problem is caused by stationary echoes (clutter). Particle filtering can help in this situation. It is a technique which implements a sequential Bayesian estimation by using Monte-Carlo methods. Particle filtering is commonly known to be used in localization applications and tracking in dynamic scenarios [18]. The estimation uses a movement model to incorporate the temporal correlation of the change of unknown parameters.

The Bayesian estimator finds unknown parameters x_k (signal delays) from a set of measurement signals $z_{1:k}$ using a posterior density function $p(x_k|z_{1:k})$. It is very common that the algorithm is processed in a recursive manner. In summary, the algorithm consists of a 'prediction' phase and an 'update' phase, where the prior density $p(x_k|z_{1:k-1})$ and the posterior density $p(x_k|z_{1:k})$ are estimated every time step k.

Prediction:

$$p(\boldsymbol{x}_k|\boldsymbol{z}_{1:k-1}) = \int p(\boldsymbol{x}_k|\boldsymbol{x}_{k-1})p(\boldsymbol{x}_{k-1}|\boldsymbol{z}_{k-1})d\boldsymbol{x}_{k-1} \tag{9}$$

Update:

$$p(\boldsymbol{x}_k|\boldsymbol{z}_{1:k}) = \frac{p(\boldsymbol{z}_k|\boldsymbol{x}_k)p(\boldsymbol{x}_k|\boldsymbol{z}_{1:k-1})}{p(\boldsymbol{z}_{1:k}|\boldsymbol{z}_{1:k-1})} \tag{10}$$

We can see that the likelihood function $p(\boldsymbol{z}_k|\boldsymbol{x}_k)$ and the movement model $p(\boldsymbol{x}_k|\boldsymbol{x}_{k-1})$ are important items in Bayesian estimation. Unfortunately the posterior density is usually intractable but there are several ways to implement the algorithm. Particle filtering deals with this problem by using samples (particles) with associated weights to represent the posterior density. If the number of particles is sufficiently large, the estimates reach optimal Bayesian estimation.

A setup consisting of a bistatic UWB transceiver and a moving metal plate is used for demonstrating the use of particle filtering in IR-UWB tracking. A 5th derivative Gaussian impulse fitting to the FCC mask is used and the repetition rate is 200 MHz (i.e. $T_s = 5$ ns). The corresponding distance is 75 cm. The metal plate moves periodically within 5 mm range. A schematic block diagram of the setup is shown in Fig. 32(a). The receive signal consists of two main contributions which can be seen in each period, corresponding to two-path propagation on the channel. The first path is the direct path between the transmit and the receive antennas (direct coupling signal). This signal has very strong visible ringing due to signal reflection from the impedance mismatch. The second signal is a signal reflected from the moving metal plate. An example of a receiving signal with a target 30 cm away is shown in Fig. 32(b). More details about the setup can be found in Sec. 4.1.

(a) Measurement setup   (b) Receive signal
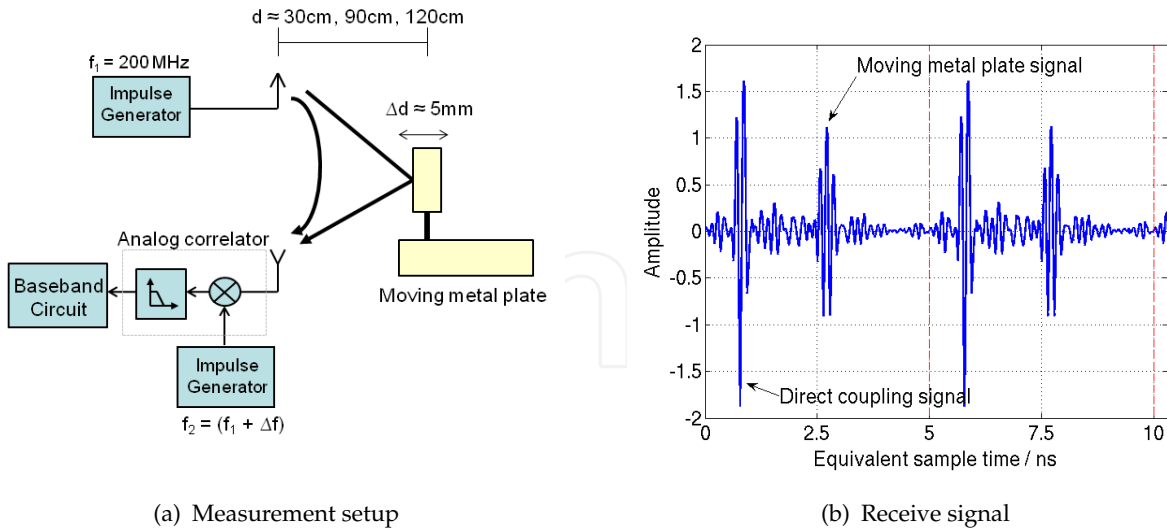
Figure 32. Measurement setup for target movement tracking and example of a periodic receive signal after the correlator.

Particle filtering with a 2-path model is used for tracking the transmission delay of the two paths. The signal after the impulse correlation can be represented in discrete-time in each

period and is considered as measurement signal z_k. The delay of each paths form the state vector x_k. More details on the setup can be found in [36].

In the following, tracking results for a moving metal plate with distances of approximately 90 cm and 120 cm are discussed. Since the distance of ambiguity for the measurement setup is 75 cm, we use the knowledge that the target is in the 75-150 cm range. This is sufficiently large for our target application. The reflected signal appears one period after the original impulse was transmitted. Particle filtering with 1000 particles is considered and the results are compared with a conventional maximum tracking method. The movement of the first path (direct coupling) and the second path (metal plate) are tracked simultaneously.

We first consider a setup with the moving target at approximately 120 cm. An example for one period of the receive signal is shown in Fig. 33(a). The reflected signal is located at around 8.8 ns. In this example, the reflected signal can be easily recognized. Fig. 33(b). shows the tracking results of the moving metal plate from both methods (particle filtering and maximum tracking for comparison). The tracking results fit well with each other and the small movement of 5 mm was estimated correctly. We can see that the particle filtering is more robust. This improvement comes from the fact that the movement model incorporates the temporal correlation of the change of the channel delays in different time steps. The conventional method does not use this information and the results can change rapidly. The particle filter needs some iterations to converge to the correct estimate.
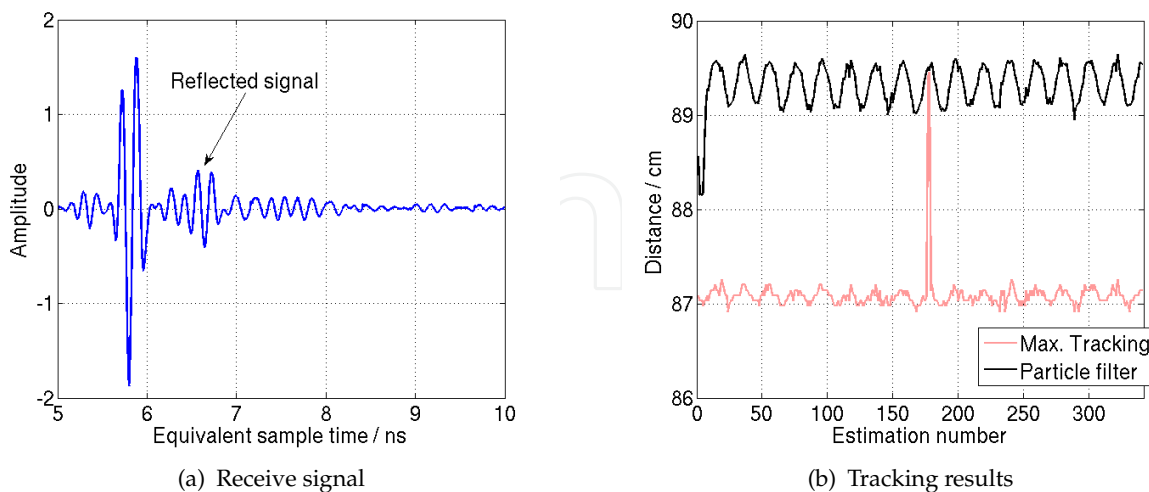

| (a) Receive signal | (b) Tracking results |
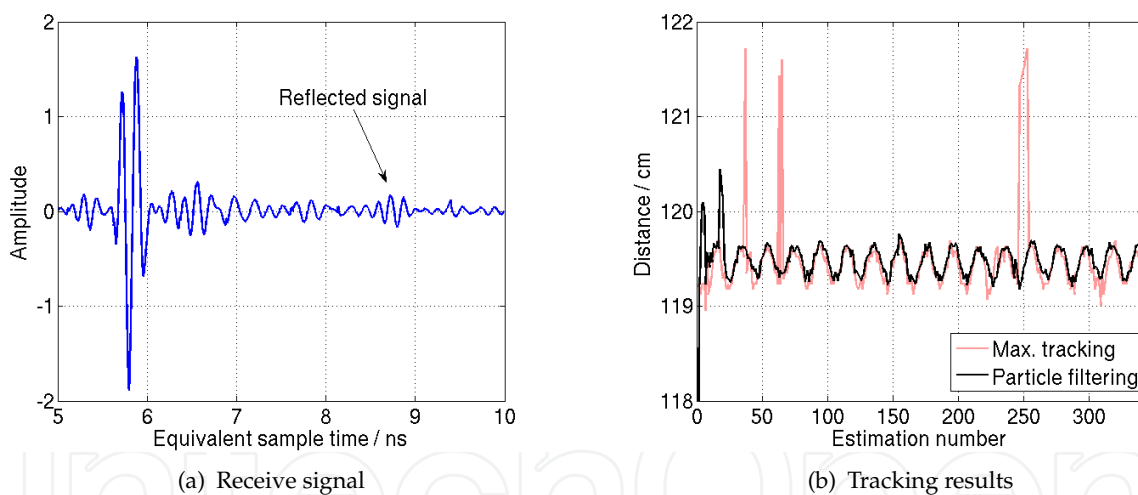
Figure 33. Receive signal with target distance ≈ 120 cm and tracking result for target distance ≈ 120 cm from conventional maximum tracking and particle filtering.

In this part, we consider the case where the noise is strong and the peak of the signal cannot be easily identified. To reduce the SNR of the signal, Gaussian noise was added to the measurement data of the previous part, so that the SNR was approximately 0dB. An example for one period of the receive signal z_k is shown in Fig. 34(a). We can see that the target signal is not clearly visible anymore and the peak value is disturbed strongly by noise. The tracking results are shown in Fig. 34(b). The conventional method does not work. The particle filtering still gives good estimates, because it does not consider only the maximum point in the target signal but the waveform as a whole. The movement model also plays a role in this improvement.

(a) Receive signal
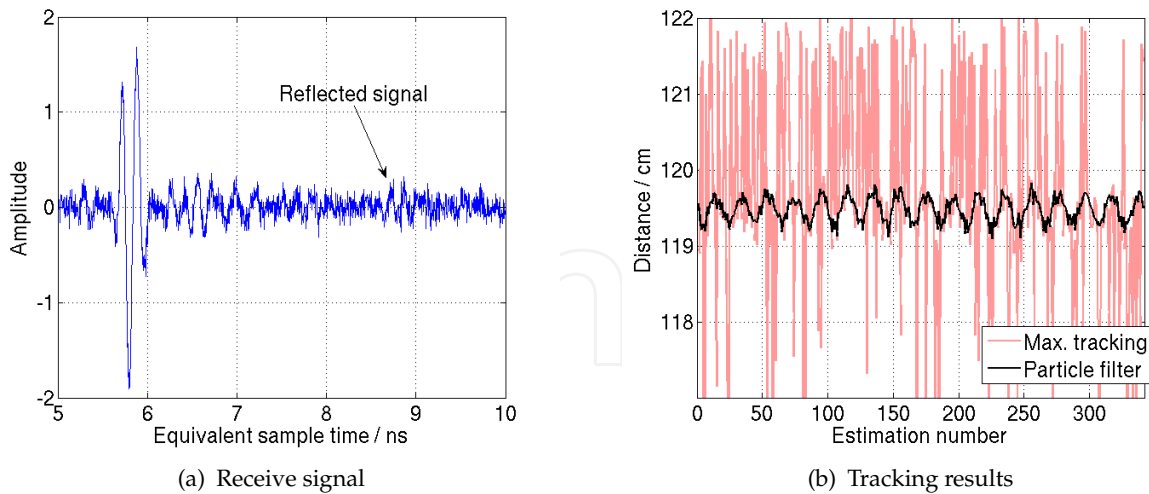
(b) Tracking results

Figure 34. Receive signal with target distance ≈ 120 cm with additional noise and tracking result for target signal ≈ 120 cm with additional noise from conventional maximum tracking and particle filtering.

Now we consider the tracking of the reflected signal for the moving metal plate at a distance of 90 cm. An example of a receive signal is shown in Fig. 35(a). We can see that the target signal is in the same interval as the ringing of the direct coupling signal. The amplitudes of the target signal and the ringing are comparable. It is not easy to distinguish between these two signals anymore. This is the same situation as in radar where we have cluttering. It can cause a bias to the estimation. A comparison of the tracking results from maximum tracking and particle filtering is shown in Fig. 35(b). We can see that the maximum tracking performs very badly because of the bias. The tracking results from particle filtering are very good. The use of the multipath propagation model eliminates the error bias given by the clutter (direct coupling).

(a) Receive signal

(b) Tracking results

Figure 35. Receive signal with target distance ≈ 90 cm and tracking result for target distance ≈ 90 cm from conventional maximum tracking and particle filtering.

Usually, the drawback of the particle filter is its complexity. In the applications considered here, this drawback is not so serious, because our system model is relatively simple. Using

particle filtering in parallel with conventional methods and exchange information between both methods can also help to reduce complexity.

3.4. Surface estimation and subsurface localization algorithms

In this section we present algorithms which can be applied for the localization of actively transmitting beacons inside of the human body. The targeted application is the tracking of catheters equiped with UWB transmitters. In this context, the use of active transmitters would mitigate the challenges related to the high attenuation of electromagnetic waves in human tissue, which makes purely passive localization extremely difficult [3].

A similar approach has been investigated in the field of ultrasonics, where catheter-mounted ultrasound transducers in combination with external arrays of imaging transducers are used to track the catheter position [25]. The advantage of UWB catheter localization is a contactless measurement setup with receivers placed in air around the patient while ultrasound transducers have to be placed directly on the body.

In subsurface imaging and localization problems, where sensors are not directly in contact with the medium, the permittivity contrast between air and the medium cannot be neglected as it leads to a different wave propagation velocity inside of the material. In case of medical applications, a relative permittivity of human tissue between 30 and 50 in the FCC UWB frequency range has to be considered [13]. UWB signals are therefore strongly reflected at the air-to-body interface. These reflections are beneficial to surface estimation applications using UWB pulse radars. For in-body localization, however, they constrain a signal emission from inside of the body. In order to overcome the strong reflection losses, we therefore propose a system that combines an active transmitter inside of the body with an array of radar transceivers outside of the body. The sensor array acts as both a surface scanner and a receiver recording the time of arrival (ToA) of a signal transmitted from inside of the body. A determination of the exact body shape prior to localization is necessary to cope with refraction effects at its surface and the change of wave propagation speed from air to tissue. This distiguishes the proposed in-body localization method from most through-dielectric localization problems like through-the-wall imaging where a plane boundary between air and the target medium is assumed [1].
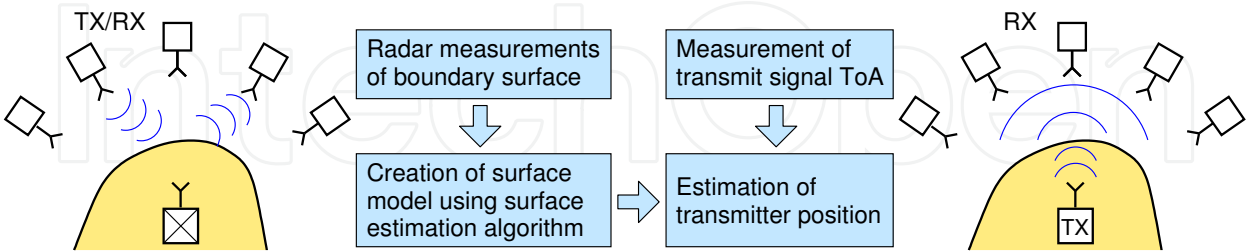
Figure 36. Proposed localization procedure of a transmitter buried in a dielectric medium. In the first step the sensor array is used to scan the surface (left), in the second step it only receives the signal transmitted from inside of the medium (right).

Fig. 36 summarizes the proposed localization approach of a transmitter placed in a dielectric medium. In a first step, the array of radar sensors is used to measure the distance to the boundary surface. These measured distances together with the known antenna positions are the input of the surface estimation algorithm which returns a model of the boundary surface.

In the second step, the transmitter inside of the dielectric is switched on and the radar sensors operate in receive mode recording the time of flight of the transmitted signal. Finally, we analyze all the acquired data and determine the position of the transmitter.

Several methods to estimate the surface of a highly reflective medium using UWB pulse radar sensors have been investigated in recent years [17, 29]. Some of these imaging algorithms, however, need extensive preprocessing of the measurement data or suffer from high complexity and computation time. In the first part of this section, we derive a simple and easy to implement 3D surface estimation algorithm based on trilateration. In the second part, building on this surface estimation method, we present an approach for the localization of transmitters inside an arbitrarily shaped dielectric medium taking into account its surface profile.

3.4.1. Surface estimation algorithm based on trilateration

Radar measurements with quasi-omnidirectional antennas only provide information about the target distance, but not about its direction. This makes surface imaging an inverse problem which can only be solved by combining measurement results from different antenna positions. In this context, target ranging using trilateration means determining the intersections of spheres, the radii of which correspond to measured target distances. The underlying assumption for using trilateration as a surface estimation method is that two neighboring antennas are "seeing" the same scattering center. As with other imaging algorithms this assumption can lead to inaccuracies of estimated target points.

The imaging principle shall first be explained using a two-dimensional example. Fig. 37(a) shows the measurement scenario of a linear array of monostatic radar transceivers arranged along the x-axis scanning the surface of a target in z-direction. Each array element measures the distance to the closest point on the target. Two exemplary measurement points X_n and X_{n+1} are picked out, and semi circles with radii corresponding to the measured target distances are plotted around the antennas. The estimated surface point is the intersection of the two circles.

(a) 2D imaging principle   (b) Top view of 3D imaging setup
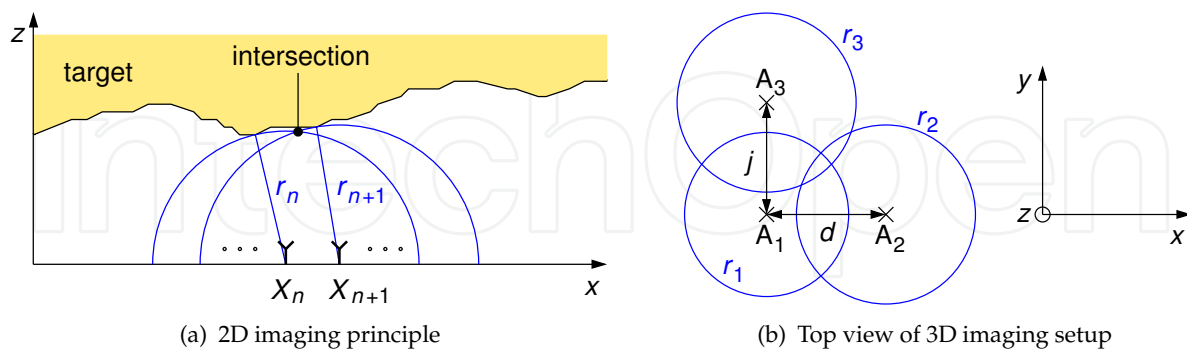
Figure 37. Cross section of a 2D imaging problem using a linear array of monostatic radar transceivers along the x-axis (a) and top view of a 3D imaging setup showing three measuring points of an antenna array in the x-y-plane (b).

Three-dimensional imaging demands for a third antenna position located in a different dimension. This setup is shown as a top view in Fig. 37(b). At each of the three positions

a target distance r_i is measured which leads to a set of spheres with radius r_i around the respective antenna position A_i, as defined by the system of equations

$$r_1^2 = \quad x^2 \quad + \quad y^2 \quad + z^2, \tag{11}$$

$$r_2^2 = (x-d)^2 + \quad y^2 \quad + z^2, \tag{12}$$

$$r_3^2 = \quad x^2 \quad + (y-j)^2 + z^2, \tag{13}$$

where d and j are the distances between two antennas in x- and y-direction, respectively. For simplicity, the first antenna position A_1 shall be at the center of the coordinate system. The above equation system is valid for a planar antenna array. In case of a curved antenna array an offset z-value has to be inserted.

The initial assumption that all three antennas are "seeing" the same target has to be assured by comparing the measured target distances r_{1-3}. If the difference between these distances is small enough, the assumption can be considered valid. For the above equations this precondition can be formulated as follows:

$$|r_1 - r_2| \leq T_{s,x} \quad \text{and} \quad |r_1 - r_3| \leq T_{s,y} \tag{14}$$

A threshold T_s in the range of about half the antenna distance has shown good results.

If the conditions in (14) are fulfilled, the target surface point of interest can be calculated by intersecting the three spheres. The coordinates (x, y, z) of the intersection are

$$x = \frac{r_1^2 - r_2^2 + d^2}{2d}, \tag{15}$$

$$y = \frac{r_1^2 - r_3^2 + j^2}{2j}, \tag{16}$$

$$z = \pm\sqrt{r_1^2 - x^2 - y^2}. \tag{17}$$

These coordinates are offsets refering to the position of the first antenna A_1. The sign in (17) depends on the arrangement of the radar transceivers. Here, we assume that the antennas are oriented towards positive z-values.

The necessary steps of the presented trilateration algorithm can be summarized as follows:

1. Pick three neighboring measurement points in two different dimensions (here: along the x- and y-axis).

2. Extract the target distance from the recorded radar measurement data at each antenna position. Multiple target responses per measurement are possible.

3. Check if the differences between the measured distances satisfy the trilateration condition in eq. (14).

4. If the previous condition is fulfilled, calculate the target coordinates using eq. (15)-(17).

5. Repeat the two previous steps if higher order reflections exist, or otherwise start over with the next three measurement positions.

3.4.2. Subsurface localization algorithm

The given parameters of the localization problem are the shape of the dielectric medium containing the transmitter, its distance to the antenna array and the ToA of the localization signal at each array element. Since all the wave propagation effects are reciprocal, our problem can also be regarded in a reverse way: At each receiver position the transmission of a short pulse with a delay corresponding to the respective previously measured ToA is assumed. In order to get the original beacon position we have to find the spot where all these virtual pulses would superimpose, i.e. the intersection of the impulse wavefronts inside of the medium [27].

According to the Huygens-Fresnel principle a refracted wavefront can be represented by an infinite number of spherical waves which originate from points on the boundary surface reached by the incoming wave. This is shown in Fig. 38(a) for a pulse transmitted from an antenna at position (3,0) towards a dielectric half space. In this 2D example, 20 source points of radial waves on the dielectric surface are considered. The radii $r_{i,n}$ of the secondary waves are calculated from the measured ToA at the receiving antenna and the length of the ray $p_{i,n}$ between the respective antenna position n and surface point i:

$$r_{i,n} = \frac{1}{\sqrt{\varepsilon_\mathrm{r}}} \left(c_0 \cdot \mathrm{ToA}_n - p_{i,n} \right), \tag{18}$$

where c_0 is the speed of light. The division by $\sqrt{\varepsilon_\mathrm{r}}$ accounts for the different wave propagation speed in the dielectric medium. The envelope of all radial waves corresponds to the wavefront we are looking for. By repeating the procedure for every antenna element of the receiver array we get a set of wavefronts as illustrated in Fig. 38(b). Finally, we determine the intersection of these wavefronts to obtain the transmitter position inside of the medium. A 3D localization problem is solved in an analog way with envelopes of spheres leading to intersecting 3D wavefronts. Here, however, the derivation of the localization procedure shall be limited to the 2D case because of simpler graphical representations.


(a) Determination of single wavefront   (b) Localization by intersecting wavefronts
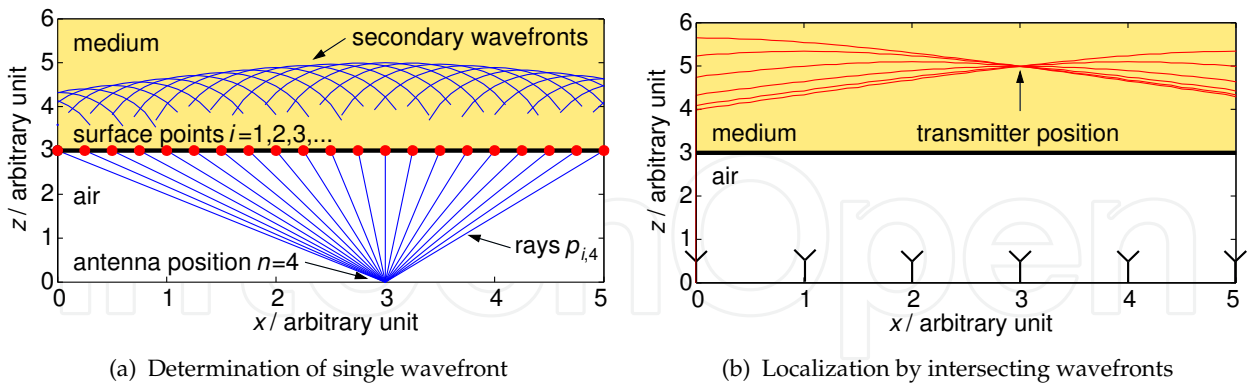
Figure 38. Determination of the 2D wavefront shape inside a medium with $\varepsilon_\mathrm{r} = 30$ for a signal transmitted in air at position (3,0) by evaluating the envelope of radial secondary wavefronts (a). Intersections of wavefronts corresponding to six different antenna positions indicate the transmitter location at (3,5) (b).

The wavefront shapes in Fig. 38(b) agree with the hyperbolic approximation of wavefronts in dielectric half spaces [28]. With more complex boundaries, however, the analytical calculation of refracted wavefronts is no longer practical, while the approach presented here is independent of the surface shape. An example of a transmitter placed behind a more complex

surface is presented in Fig. 39. The times of flight between the transmitter at (5 cm,5 cm) and the individual elements of the receiver array at $z = -20$ cm are calculated using electromagnetic field simulation software [6].
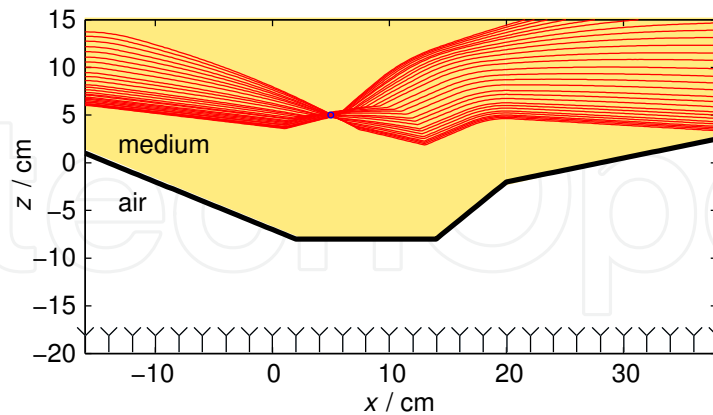
Figure 39. Calculated wavefronts in a medium with ε_r=10 based on EM field simulations. The receiving antennas are placed along the x-axis at z=-20, the transmitter is positioned at (5 cm,5 cm).

The above mentioned 2D localization procedure leads to a belt of refracted wavefronts with a focussing point where the receiver has been placed in the simulation. To decrease calculation time it is also possible to search for the narrowest point in the wavefront belt instead of calculating the intersections. This leads to an estimated transmitter position of (4.60 cm,4.94 cm), having an error of about 4 mm.

It is obvious that in the example of Fig. 39 a smaller number of wavefronts and thus less receiving antennas would be sufficient for a successful localization of the transmitter. But in practical applications this high number of antennas might still be required as a dense sensor array is rather needed for surface estimation than for solving the localization problem.

4. Systems design and measurement results

### 4.1. Single-ended bistatic radar system

At first a single-ended radar demonstrator was developed in the project, with which the potential of impulse-radio UWB sensing is evaluated. The demonstrator is built combining commercially available components for the low frequency operation control and components tailored for UWB operation dealing with the signals in the 3.1-10.6 GHz band. The UWB components are developed and fabricated in the aforementioned SiGe HBT production technology. A block diagram of the single-ended bistatic radar system is depicted in Fig. 40. The sensor uses separate antennas for transmitter and receiver to avoid losses due to power divider structures on the feedline of a single transceiver antenna. Besides a heavy crosstalk into the low-noise amplifier (LNA) of the receiver is avoided by using two antennas.

An ultra-broadband Vivaldi antenna is chosen, which consists of an exponentially tapered slot on a microstrip substrate. The transition from microstrip to slot line is done by a Marchand balun, as discussed in [22]. On the feeding line of the transmit antenna an impulse generator IC is mounted, which emits an impulse with a shape very similar to the fifth derivative of a Gaussian bell shape with a standard deviation $\sigma = 51$ ps. This impulse shape fits into
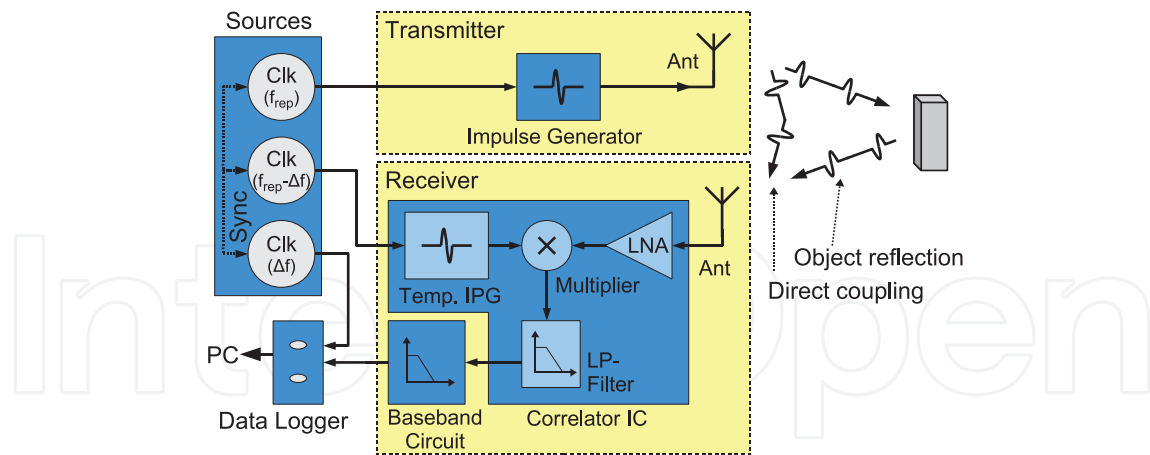
**Figure 40.** Block diagram of the single-ended bistatic radar system.

the 3.1-10.6 GHz UWB spectral mask allocated by the FCC in the United States and has a voltage amplitude of 600 mV peak-to-peak [8]. The impulse generator radiates an impulse at every rising slope of an input trigger signal. Here a sinusoidal signal is used to trigger the impulse generator, so at every rising edge of the sinusoidal signal an impulse is emitted which results in a continuous impulse train. The sinusoidal signal is supplied from one source of the direct-digital-synthesizer (DDS) AD9959. All four clock sources of the AD9959 (three are used) are synchronized among each other to allow a phase and frequency stable operation between the signals. The transmitter is adjusted to generate an impulse train with a repetition rate of $f_{rep} = 200$ MHz. To reduce impulse-to-impulse jitter, spurious emissions of the 200 MHz sinusoidal trigger signal are filtered by a narrowband helix filter. The generated impulse train is continuously radiated by the antennas, is reflected at the desired object and enters the receiver. The reflection at the object causes a phase inversion to the impulses, therefore it is received with inverted amplitude. Additionally the impulse train is fed to the receiver by a direct and non-inversed coupling between the antennas.
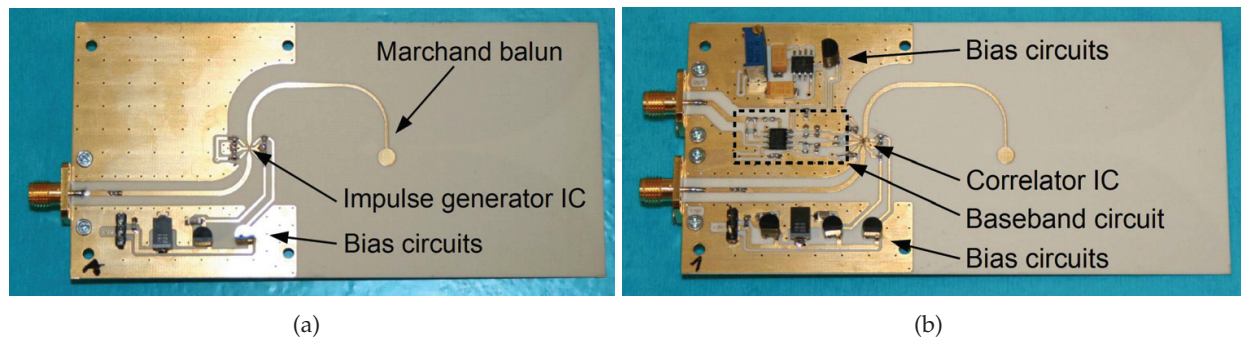
Figure 41. Picture of (a) Vivaldi transmit antenna with mounted impulse generator IC and (b) Vivaldi receive antenna with correlator IC and baseband circuit.

These signals are processed in the receiver by a monolithic correlator IC, which consist of a UWB LNA, a four-quadrant multiplier, a template impulse generator generating a fifth Gaussian derivative impulse corresponding to the transmit impulse, and a first integrating low-pass filter with a cut-off frequency of 800 MHz [9]. The template impulse generator is driven by a second clock source of the AD9959 at a repetition rate of

$f_{rep} - \Delta f = 200\,\text{MHz} - 25\,\text{Hz}$. This sinusoidal clock signal is filtered as well with a helix filter to improve jitter performance. The output signal of the correlator IC is processed with a baseband circuit, where it is amplified and further integrated by a low-pass filter with a cut-off frequency of 25 kHz. After this it is fed to a data-logger, which samples the generated signals with a sampling period of 30 μs and transfers them to a PC for further processing. Additionally a synchronizing signal of $\Delta f = 25\,\text{Hz}$ from the third DDS clock signal is sampled

(a)   (b)
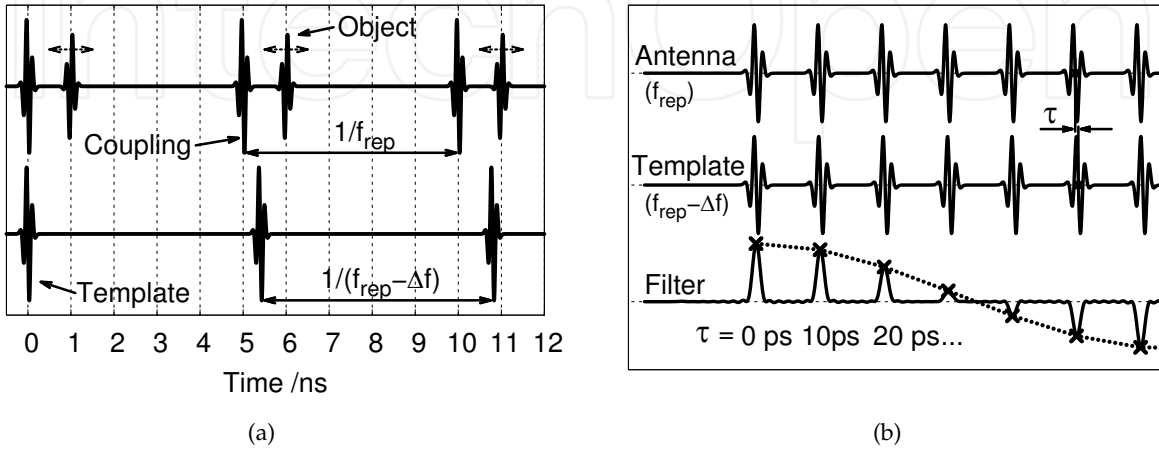
Figure 42. (a) Illustration of the template impulse sweeping through the antenna receive signal. (b) Illustration of the evolving correlation signal from receive and template signal in the region where the impulses overlap.

and transferred to the PC as well. In the PC a post-processing of the continuous data stream is done using a custom software written in Lab Windows/CVI. Pictures of transmit and receive antenna with mounted components are shown in Fig. 41. A detailed description and supporting measurements of the hardware can be found in [7, 31].
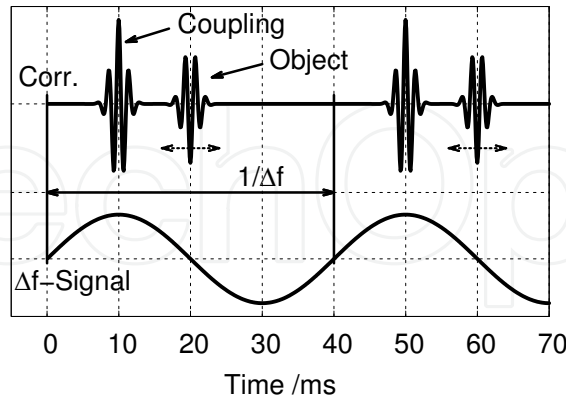
Figure 43. Illustration of the correlation signal at the receiver antenna output port, together with the Δf-signal for separation of the repetition.

To determine the distance between sensor and desired object and the variation of the distance between them, a time-of-flight measurement is applied using a sweeping impulse correlation as explained in [10]. The sweeping impulse correlation is very similar to an undersampling technique and avoids high-speed sampling of the gigahertz-range UWB impulses. This

method is illustrated in Fig. 42 by showing the signals appearing in the receiver. In the upper trace of Fig. 42(a) the received signal at the output of the LNA in the correlator IC is shown. An impulse from both, the non-inverted direct coupling and the inverted reflection at the object is shown. The impulses are repeated at the repetition rate f_{rep}. The template impulse in the correlator IC, shown in the lower part of Fig. 42(a), is operating at a repetition rate $f_{rep} - \Delta f$. Therefore it is continuously changing its time alignment to the received signals and appears sweeping through the impulse sequence.

(a)   (b)
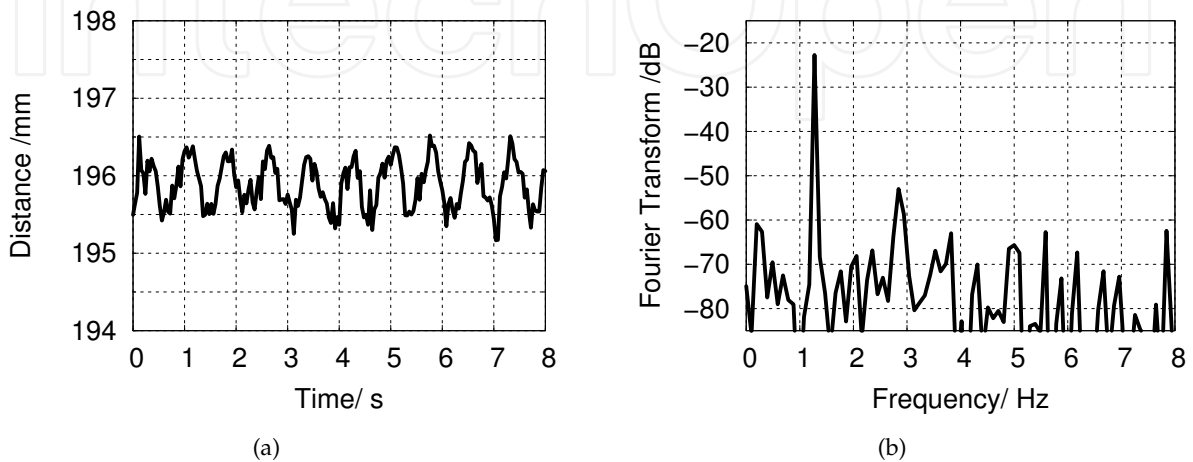
Figure 44. Measurement of sinusoidally moving metal plate placed in front of the antennas at a distance of 19.6 cm and a deviation of approx. 1 mm in (a) time and (b) frequency domain.

(a)   (b)
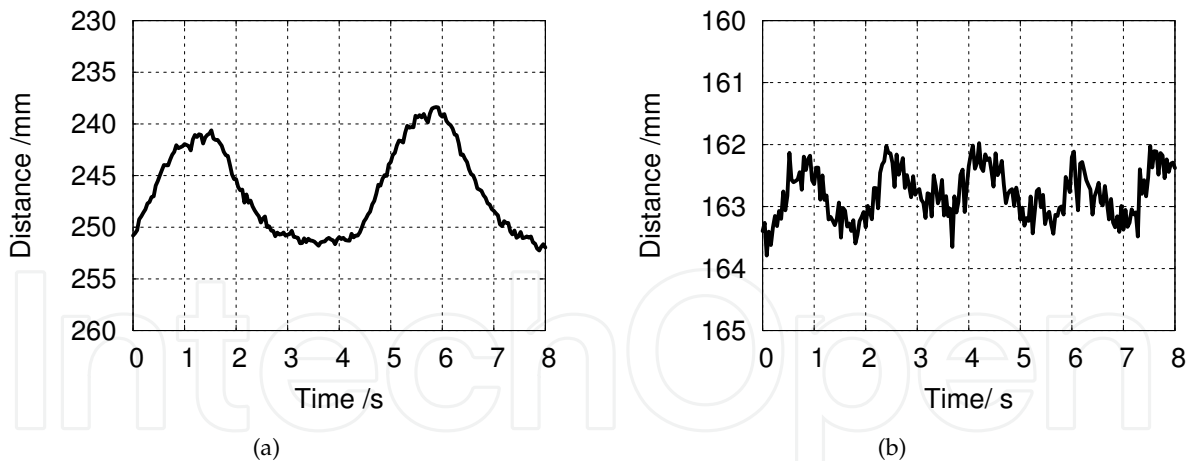
Figure 45. Time domain breathing measurements of (a) a male test person lying on the back and (b) a seven-week old child sleeping in bed.

At each position of the impulses the cross-correlation is computed by multiplying the signals and integrating them. This operation can be seen in Fig. 42(b) in the region where one received impulse and the template impulse are overlapping each other. The lower part of the figure illustrates the output of both filters. The solid line represents the output signal of the 800 MHz filter which integrates each single impulse. The dashed line shows the output signal of the baseband filter with a cut-off frequency of 25 kHz, which integrates a multitude of single

impulses. By this procedure, a cross-correlation curve of two fifth Gaussian derivatives is developing. The correlated curve of the above illustration example is depicted in Fig. 43. The correlation impulses from the direct coupling and the reflection at the object can be distinguished. As discussed, the reflection at the object is mirrored, because the impulse is inverted by the reflection. This signal is present at the output of the receive antenna and is sampled by the data-logger. The correlation signal is continuously repeated with a repetition rate of Δf. For a separation of the correlation sweeps, the Δf-signal is sampled as well by the data-logger. When the object under investigation is now moving, the part of the correlation signal coming from the object reflection is correspondingly changing its alignment to the Δf-signal and the movement can be measured. The movement determination of the object is continuously done by software in the PC. First a separation of the correlation sweeps by the rising slope of the Δf-signal is performed. Then both slopes of the correlation curves, the slope from the object and the slope from the direct coupling, are tracked and their positions continuously monitored. Tracking both slopes yielded best precision, compared to tracking the minimum of the correlation curve or only the slope of the correlation signal from the object [31].

To measure the precision of the sensor a metal plate is placed in front, which is mounted on a sledge driven by an eccentric disk, moving the metal plate forward and backward with an approximately sinusoidal deviation. Fig. 44(a) shows a time domain record of a movement measurement with the metal plate placed at a distance of 19.6 cm, a deviation amplitude of approximately 1 mm and a repetition rate of around 1.35 cycles/s. The movement is clearly resolved by the measurement. In Fig. 44(b) the calculated spectrum of the measurement can be seen. The frequency maximum is very clearly visible and verifies a precision of the demonstrator in the millimeter to sub-millimeter range.

In a further measurement the sensor is pointed to the abdomen of a male test person lying on the back at a distance of approximately 25 cm[1]. At the abdomen the largest breathing amplitude occurs. Fig. 45(a) shows a breathing measurement in case the person is breathing normally. The breathing amplitude exceeds 10 mm and the repetition rate is around 2.5 cycles/s. For a further measurement the demonstrator is placed towards a sleeping seven-week old child lying on the back at a distance of approximately 16.3 cm. Fig. 45(b) shows a rhythmic breathing period with a movement of around 1 mm in the direction of the sensor and a repetition rate of 1.5 cycles/s. These measurements show, that the sensor can be used to monitor the breathing of adults and infants lying on the back and that breathing patterns can clearly be detected using the single-ended bistatic impulse-radio UWB radar demonstrator.

4.2. Differential bistatic radar system

A differential bistatic radar system for detecting vital signs was also developed. It follows the approach described in Sec. 4.1, but with fully differential ICs as described in Sec. 2.2 and Sec. 2.3.3 and with significantly reduced power consumption. Here two dipole-fed circular slot antennas are chosen instead of the the Vivaldi antennas. Both the differential impulse

---

[1] Measurements on humans using the single-ended bistatic radar sensor have been approved by the ethic commission of Ulm University.

(a)   (b)
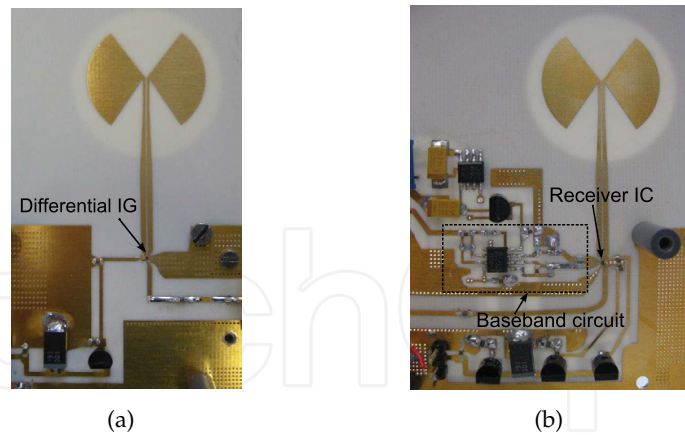
Figure 46. Photographs of transmit antenna with mounted differential impulse generator IC and the complete receiver with RF frontend IC and baseband circuit.

generator and the correlation receiver front-end are mounted chip-on-board at the feeding points of the dipole antennas. Fig. 46 shows the pictures of transmit and receive antennas with mounted differential ICs.

Using the same DDS clock generator and post-processing software as described in Sec. 4.1, the ability of the realized differential bistatic radar system for tracking a metal plate which moves back and forth with a sinusoidal deviation is demonstrated. The measured result in the time domain can be seen in Fig. 47(a). A deviation amplitude of around 1.5 mm can be


(a) Time domain   (b) Spectrum
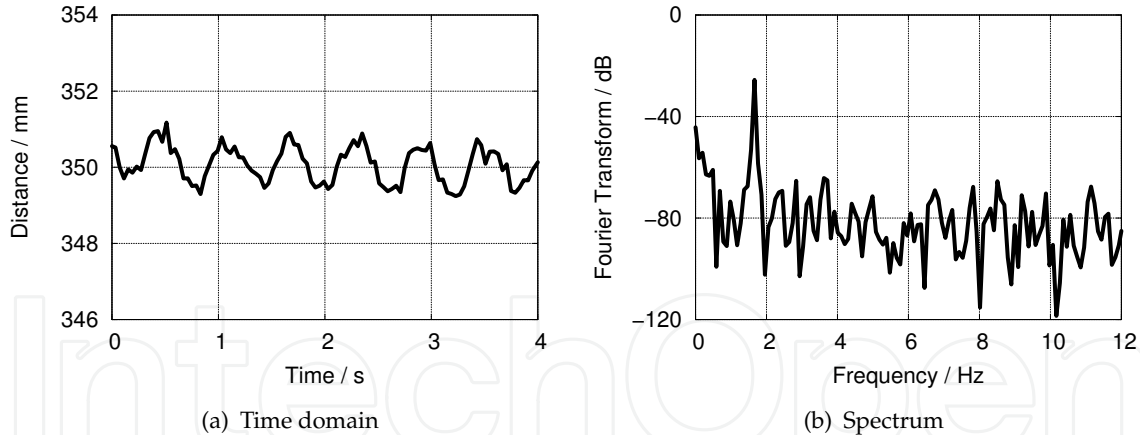
Figure 47. Measurement results of a moving metal plate in front of the bistatic radar with a distance of 35 cm in time and frequency domains.

clearly seen. Fig. 47(b) shows the calculated spectrum information of the measurement. The maximum point is clearly visible and indicates the movement frequency of the metal plate.

A common application for this radar system is the detection of vital signs. Here, an adult male with pronounced tachypnea is seated 5 cm from the radar. Fig. 48(a) shows the recorded time domain data. The breathing pattern is clearly visible and its amplitude is around 5 mm. The time domain data is Fourier transformed to frequency domain as shown in Fig. 48(b). It clearly indicates that the respiration rate is around 35/min.

(a) Time domain   (b) Spectrum
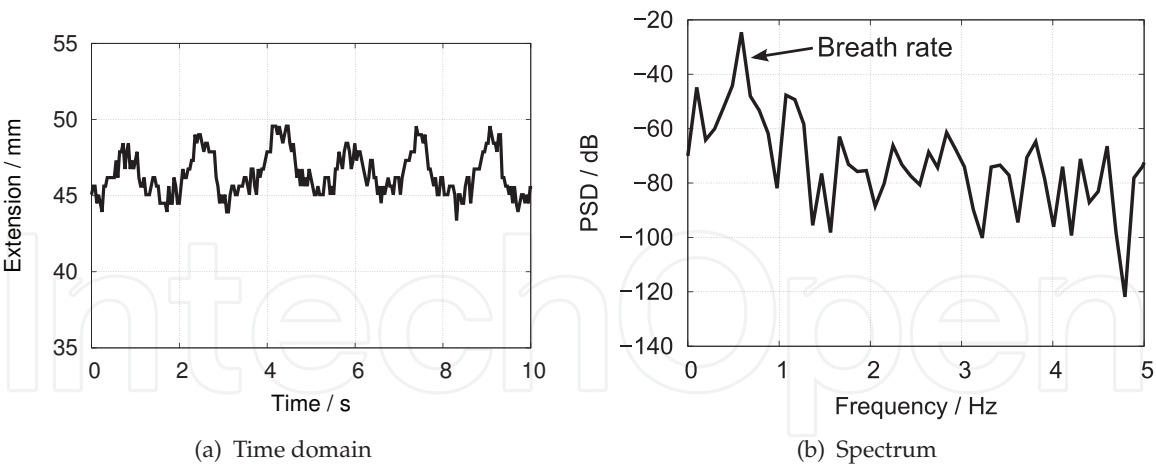
Figure 48. Time domain and frequency domain measurements of vital signs of a male test person standing in front of the bistatic radar.

In a further measurement, surface estimation of a container filled with a sugar solution whose properties are similar to those of human tissue was performed by moving the radar up and down in 2 cm steps along both the x- and y-axis. For demonstrating that the radar system is capable for this application, only the lower part of the container is scanned. The trilateration-based imaging algorithm derived in Sec. 3.4 is applied. The photograph of the container is shown in Fig. 49(a), and a cloud of estimated surface points representing the front of the target can be seen in in Fig. 49(b). The result clearly indicates the distance from the radar sensor to the container and the planar surface structure.

(a) Photograph   (b) Measurement
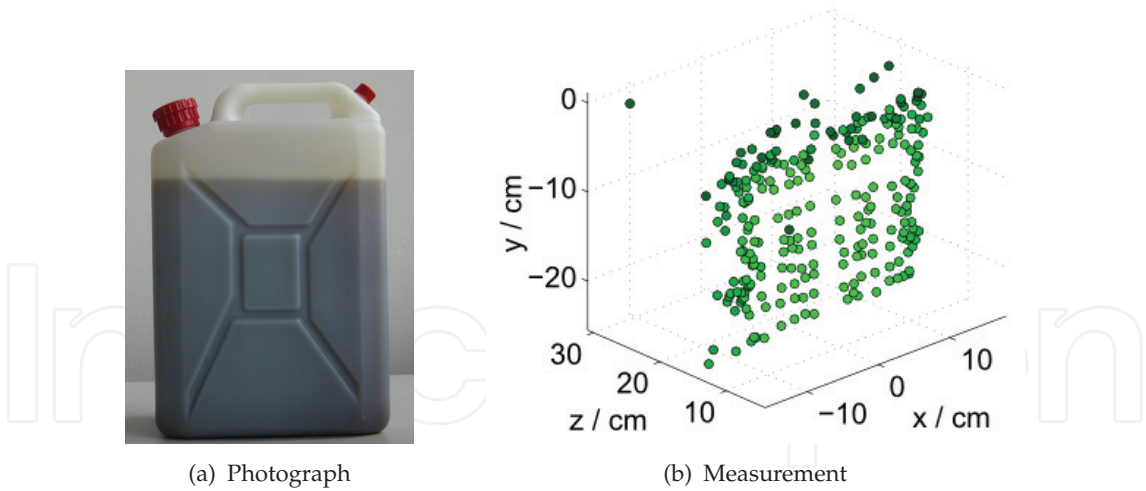
Figure 49. Photograph of the liquid container and measured cloud of estimated surface points.

4.3. Communcation with implants

In this section we address another application of UWB technology in medicine, the communication with implants. Impulse-based UWB technology is a promising solution for future implanted medical devices demanding data rates in the Mbit/s range and a low power consumption. Here, we present a demonstration system for uni-directional data transmission

between a transmitter inside tissue-mimicking liquid and a receiver placed inside or outside the medium. These two measurement scenarios are illustrated in Fig. 50.

(a) Tissue to tissue   (b) Tissue to air
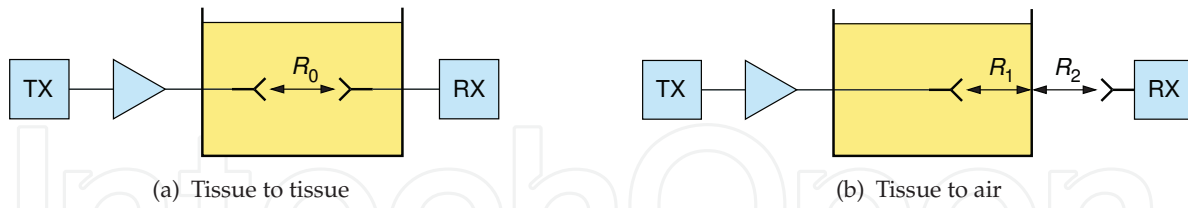
Figure 50. Measurement scenarios for the demonstration of impulse-based data transmission for implants using an energy detector. An amplifier is applied on the transmit side to cope with the high attenuation of the phantom liquid.

As discussed in Sec. 3.1, many different approaches for IR-UWB receivers are feasible. Non-coherent detection is chosen here because of the challenges regarding synchronization in coherent receiver setups and because of the dispersive properties of human tissue, which lead to unpredictable shapes of the received signals. Even though non-coherent detectors are suboptimal, they are insusceptible to dispersive effects of the channel, and therefore well-suited for communication with implants.

The simplest non-coherent receiver concept is an energy detector, which basically consists of a squaring device and an integrator (see Sec. 2.3). Besides its simplicity, the advantage of an energy detector is that possible narrow-band interferers within the operating frequency band could be suppressed by using the comb filter approach described in Sec. 3.2. This would improve the SNR additionally. Hence, the energy detector is chosen as the receiver in the demonstration setup for communication with implants. In this demonstration, on-off keying is used as the modulation scheme and a unidirectional transmission with a data rate of 100 Mbit/s is selected. This data rate and a unidirectional transmission are sufficient for most medical applications.

The transmitter in Fig. 50 consists of a UWB impulse generator (IG) and an antenna. The transmit data are generated externally by a bit pattern generator, clocked by a signal generator. The receiver topology is the same as shown in Sec. 2.3.2, but in a single-ended configuration. The output signal is amplified and displayed on an oscilloscope. For further signal processing in the digital domain, a comparator circuit with a properly adjusted threshold voltage can be applied. A more detailed description of the transmitter and receiver structures used can be found in [21].

To demonstrate the transmission in an environment similar to human tissue with a highly dispersive and lossy behavior, two antennas are immersed in a tissue-mimicking liquid. This liquid consists mainly of sugar and water. The properties of the liquid are similar to skin tissue with a relative dielectric constant ε_r of 28 at 7 GHz and an attenuation of about 22 $\frac{dB}{cm}$. The influence of the dispersive behavior on the impulse shape is illustrated in Fig. 51 in time and frequency domain. There, the output signal after the transmission through the phantom liquid is shown in comparison to the input signal. Due to increased losses for higher frequencies, the impulse shape is significantly broadened and the amplitude is decreased by approximately 60 dB for the used path distance of 23.5 mm between the two immersed antennas.

(a) Time domain

(b) Frequency domain
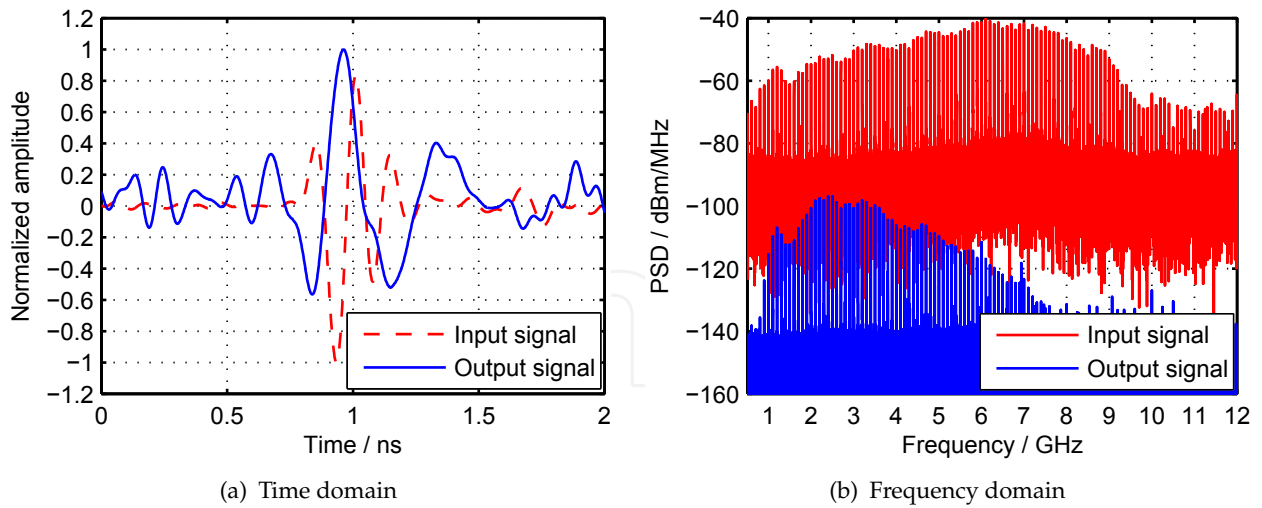
Figure 51. Typical received signal after the transmission of an impulse through tissue-mimicking liquid. The distance between transmitter and receiver is $R_0 = 23.5\,\text{mm}$.

A data transmission is still achievable in these cases as illustrated by the reception of a typical bit pattern in Fig. 52(a). To this end, an additional amplifier with 12 dB gain is inserted after the impulse generator in order to compensate for the high losses. This measurement setup demonstrates the transmission from a deeply implanted device to a reading device placed directly on the human body, e.g. applicable for capsular endoscopy. In a final scenario, the communication of a less deeply implanted device with a base station outside the human body is considered. There, one antenna is immersed in the phantom liquid and a second one is located outside in free space (see Fig 50(b)). In this setup, the distance of the immersed antenna to free space is fixed to 15 mm, and the location of the outer antenna is varied. Similar measurement results as before are obtained here. In Fig. 52(b) the output voltage of the energy detector is plotted against the distance R_2 between the medium surface and receiver in air. The observed maximum distance of the base station for a reception is 15 cm, then the attenuation limit is reached.

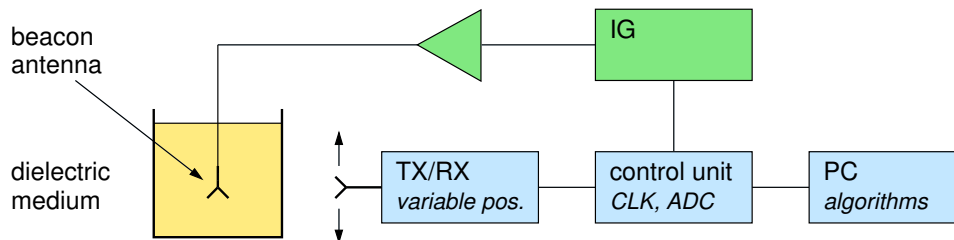## 4.4. Surface estimation and subsurface localization measurements

4.4.1. Measurement setup

For the evaluation of the surface estimation and subsurface localization algorithms presented in Sec. 3.4, measurements are performed using a similar bistatic UWB radar sensor as described in Sec. 4.1 [22] and the miniaturized antenna optimized for radiation in human tissue, presented in Sec. 2.1.3. The measurement setup is illustrated in Fig. 53. In this setup we use one single radar sensor which is emulating a whole sensor array by being moved along the x- and y-axis in front of the target. The target object is a container filled with the same tissue-mimicking liquid already used in the measurements of Sec. 4.3. A control unit providing clock signals for the radar sensor is connected to a computer where the signal processing and visualization is performed. In the measurements for subsurface transmitter localization, the upper elements of the setup in Fig. 53 are switched on. The miniaturized antenna placed inside of the tissue-mimicking liquid is now transmitting a 5th derivative of a Gaussian pulse generated by the impulse generator (IG). Because of the high loss in the

(a) Tissue to tissue

(b) Tissue to air
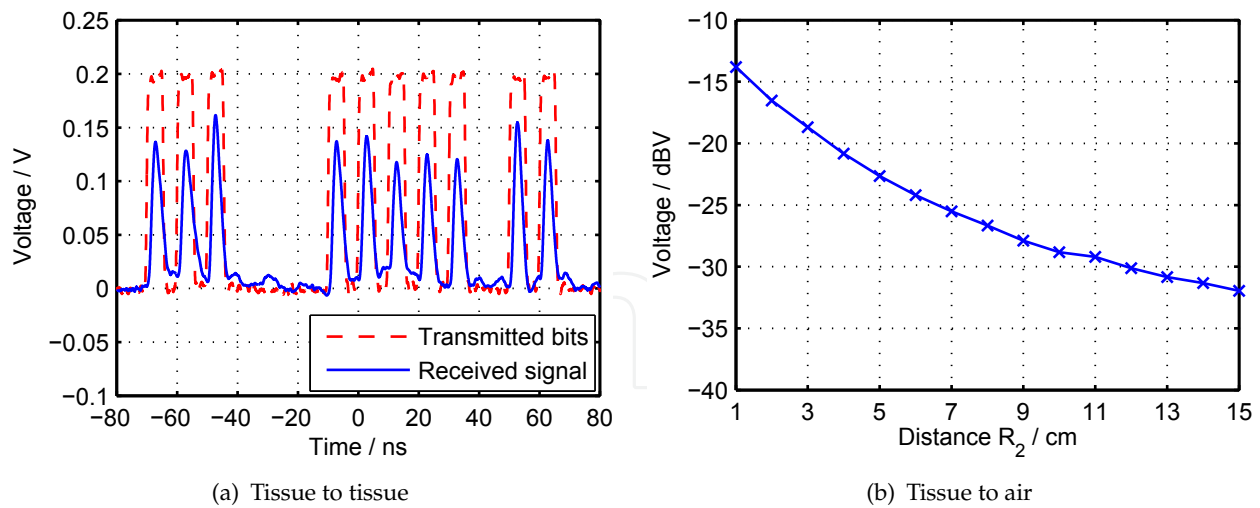
Figure 52. Measured output voltage of the energy detector according to the measurement scenarios in Fig. 50 using a data rate of 100 Mbit/s.

medium of about $22\,\frac{\mathrm{dB}}{\mathrm{cm}}$, an amplifier is used. For localization, the radar sensor outside of the container is operating in receive mode measuring the ToA of the transmitted impulse.
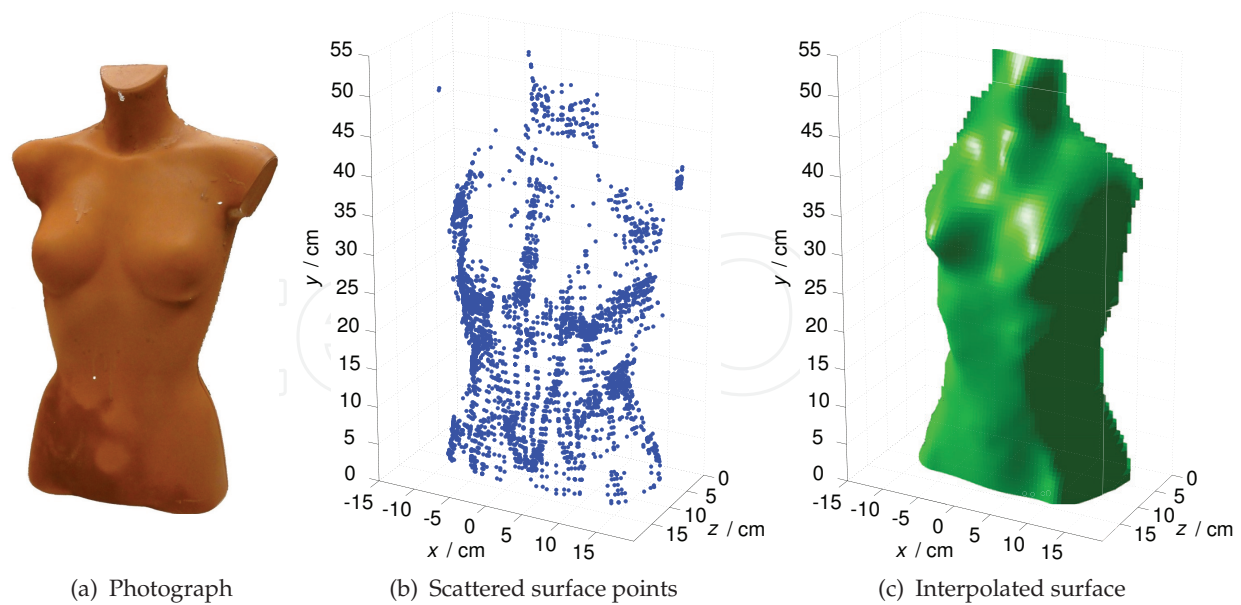

Figure 53. Measurement setup for surface estimation and subsurface transmitter localization. The radar sensor is moved in front of the liquid container to scan its surface. For localization, the upper part consisting of an impulse generator and an amplifier is switched on.

4.4.2. Surface estimation results

In 3D surface measurements the performance of the trilateration-based imaging algorithm derived in Sec. 3.4.1 is verified. As a target object a plastic dummy of a female torso of about 60 cm height as pictured in Fig. 54(a) has been chosen. In order to increase the target's reflectivity the surface of the dummy has been treated with highly conductive copper laquer. Radar scans of the 3D surface are performed by moving the radar sensor up and down in 1 cm-steps along the y-axis and by rotating the target object in 5°-steps. As a result, a cylindrical array of radar sensors is emulated.

Fig. 54(b) shows the output of the imaging algorithm, a cloud of estimated surface points representing the front side of the target. An interpolation of these points is necessary to obtain a surface model needed for the subsurface localization application. The interpolated surface is illustrated in Fig. 54(c) showing a good agreement with the original target object.

The performance of the proposed algorithm regarding its accuracy is compared to the well-established imaging algorithms "Seabed" [29] and "Envelope of Spheres" [16] by evaluating the surface measurement of a metal sphere with a known diameter of 35 cm. A

(a) Photograph   (b) Scattered surface points   (c) Interpolated surface

Figure 54. Surface estimation result of the proposed trilateration-based imaging algorithm for a radar measurement of a human torso dummy using a circular antenna arrangement.

spherical target was chosen here since a mathematical surface of the torso dummy model is unavailable. The error distance between estimated points and the ideal surface of the target sphere is calculated and plotted in Fig. 55 for different densities of measurement points. The graphs show the percentage of estimated points having a certain deviation in cm from the ideal surface. In order to compare the results of the different algorithms at exactly the same coordinates, the estimated points have been interpolated on an identical coordinate grid.

(a) Antenna distance $d = 1.5$ cm   (b) Antenna distance $d = 6$ cm
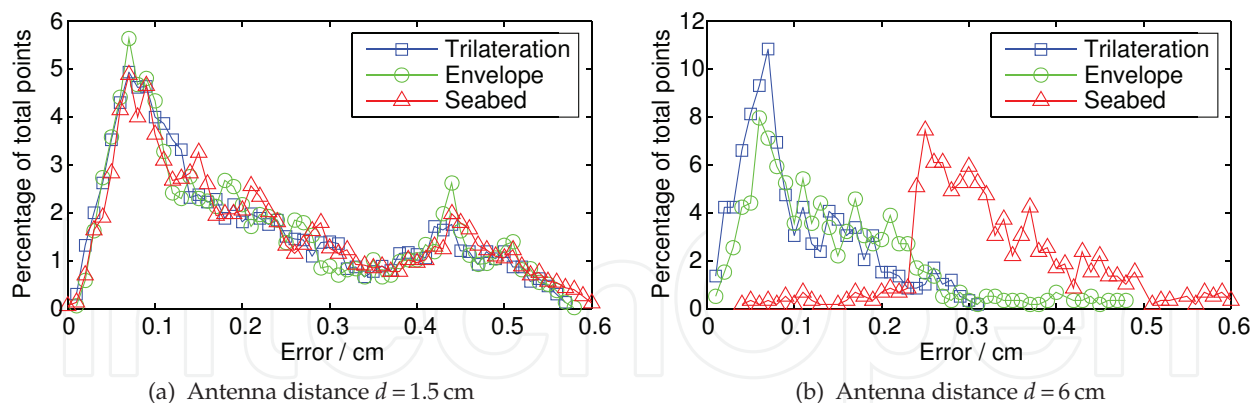
Figure 55. Percentaged distribution of the error between estimated surface points and the actual surface of a trapezoidal target using a monostatic radar setup with two different distances d between measuring points. The performance of the proposed algorithm is compared to state-of-the-art imaging algorithms.

While in the first measurement in Fig. 55(a) a relatively small step width of $d = 1.5$ cm between two measuring positions has been used, the measurement results in Fig. 55(b) show the errors obtained with a quadrupled step width of 6 cm. It can be seen that with a high density of measurement points there is no significant difference of estimation errors between the three compared algorithms. The deviations from the ideal surface points are in a low millimeter range. However, with an increased distance between measurement points the performance

of "Seabed" is degrading significantly, while the errors obtained with trilateration and the "Envelope of Spheres" algorithm remain in the same range.

It can be seen that the trilateration-based imaging algorithm achieves similar results as state-of-the-art surface estimation algorithms while the compexity is reduced since here no preprocessing of measurement data is needed. A more detailed description of the trilateration-based imaging algorithm and further measurement results can be found in [26].

4.4.3. Transmitter localization results

In the measurements for the evaluation of 3D transmitter localization, a liquid container whose concave surface roughly approximates the surface of a human body is chosen. Fig. 56 shows a top and side view of the measuring setup with the transmitter placed in a glass fish bowl of 21 cm diameter. The radar sensor is scanning in 1 cm steps in x- and y-direction emulating an antenna array with 14×11 elements in total.

(a) Top view (b) Side view
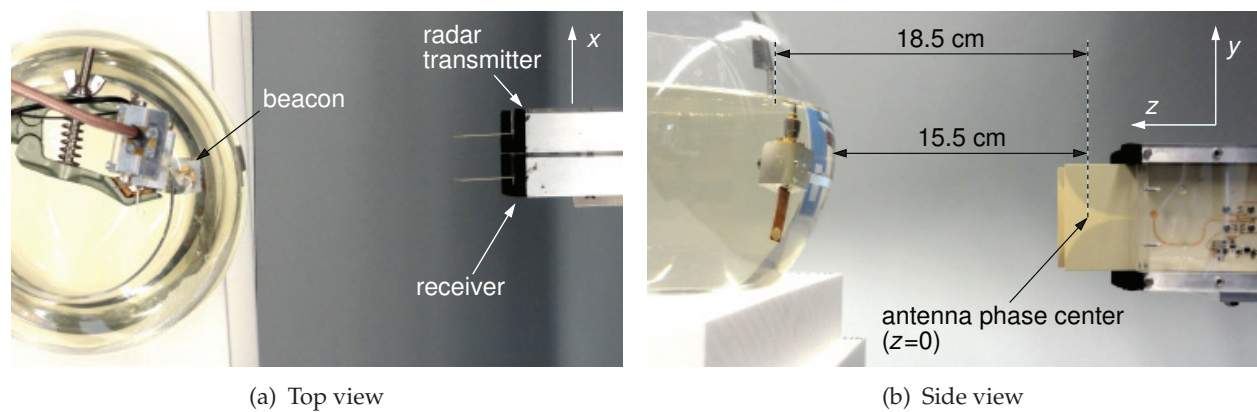
Figure 56. Photographs of the 3D measurement setup with a transmitter placed in a concave liquid container.

(a) Top view (b) Side view
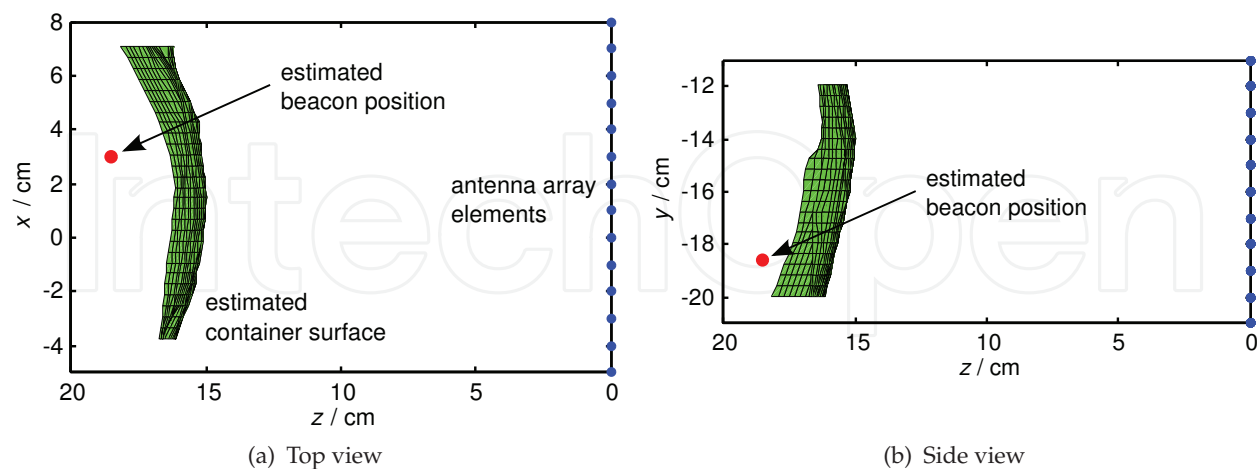
Figure 57. Measurement results in a top and side view corresponding to the photographs in Fig. 56 showing the estimated location of the beacon behind the container surface. The dots at $z = 0$ represent the sensor positions.

The surface points found by the trilateration-based imaging algorithm are interpolated to create the boundary shape depicted in Fig. 57. These graphs follow the perspectives of the

photographs in Fig. 56 allowing a rough evaluation of the localization result. By applying the localization method of Sec. 3.4.2 based on the evaluation of 3D wavefronts inside of the medium, an estimated position of the transmitter of $(x,y,z) = (3.0\,cm,-18.4\,cm,18.5\,cm)$ is calculated. Even though an exact verification of the antenna position inside of the liquid is difficult, the manually measured z-distance of 18.5 cm between the transmitter and the receiver agrees with the estimated beacon position. In the photographs of Fig. 56 the receiver antenna is positioned at the x- and y-position closest to the beacon antenna in the container. These known sensor coordinates of (3 cm,-19 cm) also coincide well with the estimated beacon position. In case of a convex surface like the fish bowl an even better localization can be expected when using a circular or spherical arrangement of the receivers around the medium, instead of a planar arrangement.

Due to the high attenuation of signals transmitted through tissue-mimicking liquid we can only localize positions close to the container surface. In our measurements the signal-to-noise ratio of impulses running through more than 3 cm of tissue-mimicking liquid became too low to be detected. One possible way to increase the maximum transmitter distance from the surface would be the use of a cascade of multiple amplifiers to realize a higher transmitter power output. Regarding the optimization of signal processing an approach based on compressed sensing is investigated to cope with lower signal-to-noise ratios at the receiver [34].

5. Conclusion

In this chapter, novel hardware components, algorithms, systems and possible approaches in the field of UWB radar and communications for biomedical applications have been presented.

Three novel UWB antenna concepts have been introduced targeting different tasks in the medical field. For communication purposes, a circular slot antenna excited with a dipole element has been presented. Its novel differential feeding concept suppresses parasitic radiation by cable currents on the feed lines. In a new concept for applications requiring directive antennas with small beamwidths, a dielectric rod has been added to the circular slot antenna, resulting in a compact and easy-to-fabricate antenna with a high mean gain of 8.7 dBi. Furthermore, a miniaturized UWB slot antenna, optimized for the radiation in human tissue has been designed.

A flexible, differential chipset using Si/SiGe HBT technology for IR-UWB applications has been presented. On the transmit side, a low power impulse generator based on cross-coupled LC oscillator is successfully realized. It generates ns-duration and stable impulses with a spectrum well fitting the FCC mask. This impulse generator has been successfully extended to include tunability to the FCC, ECC and Japanese UWB masks as well as a biphase modulation function. On the receive side, an energy detection receiver optimized for simple on-off keying communications and a correlation detection receiver for short range radar applications have been presented. Both receivers are based on a fully differential UWB low-noise amplifier and a four-quadrant RF multiplier which performs either squaring or multiplication operations.

Using the aforementioned components, two bistatic radar systems, a single-ended and a differential configuration, have been built. Their performance has been demonstrated in a setup for vital sign detection.

Regarding UWB communications, a proposal for a transmission scheme has been discussed, using a special spread spectrum method and energy detection combined with a comb filter, which improves the SNR and rejects narrowband interference. The robustness of this concept has been demonstrated for multipath propagation channels as well as for narrowband interference, noise, and synchronization errors. The approach fits well to medical applications, because small multipath delay spreading promises an easier realization of the analog time delay needed for the comb filter. A trade-off between the number of UWB impulses per symbol (bit) and the data rate requirement has to be made for different applications.

In addition, a new concept for an impulse-radio transmission based on code shift keying with a comb filter receiver has been introduced. In this concept, the delay of the analog delay element could be shorter than the channel impulse response. It has been shown and verified by simulation that the performance and the resistance against multipath propagation, noise, narrow band and multisensor/multiuser interference are the same as in the original approach with longer delays in the comb filter loop.

Simulation results have shown that particle filtering can improve the ranging and tracking performance of an impulse UWB radar substantially in scenarios with low signal-to-noise ratio and cluttering in comparison with more conventional methods. A trade-off between realization complexity and performance can be adjusted thanks to the flexibility of the proposed algorithm.

It has been shown practically that a non-coherent energy detector is a suitable receiver concept for UWB communication with implants. The energy detector operates without synchronization and is insusceptible to dispersive effects of the channel. Demonstrational measurements in tissue-mimicking liquid have been performed with a data rate of 100 Mbit/s meeting the requirements for modern medical devices.

A 3D surface estimation algorithm based on trilateration for ultra-wideband pulse radars has been presented and derived mathematically. Since this method needs no preprocessing of measurement data its implementation is very simple. In 3D surface measurements the performance of the proposed algorithm has been verified, and comparisons with established algorithms have shown a similar performance regarding estimation errors.

As a next step towards the targeted application of catheter tracking, a method for the localization of UWB transmitters buried in homogeneous dielectric media has been presented. With the aid of surface estimation algorithms a localization behind an arbitrarily shaped medium boundary is possible. For this purpose we have proposed a system consisting of an array of UWB radar sensors outside the medium and a beacon inside the medium transmitting a short UWB pulse. The external sensors serve for surface scanning and for measuring the time of arrival of the transmitted signal. The performance of the proposed localization algorithm has been verified using electromagnetic field simulations and measurements, in which a transmitter has been placed in tissue-mimicking liquid.

Author details

Dayang Lin, Michael Mirbach, Thanawat Thiasiriphet, Jürgen Lindner, Wolfgang Menzel and Hermann Schumacher
Ulm University, Germany

Mario Leib
EADS Deutschland GmbH, Division Cassidian, Ulm, Germany

Bernd Schleicher
TriQuint Semiconductor GmbH, Munich, Germany

6. References

[1] Ahmad, F. & Amin, M. G. [2006]. Noncoherent approach to through-the-wall radar localization, *IEEE Transactions on Aerospace and Electronic Systems* 42(4): 1405–1419.

[2] Belostotski, L. & Haslett, J. [2009]. A technique for differential noise figure measurement with a noise figure analyzer, *IEEE Microwave Magazine* pp. 158–161.

[3] Bilich, C. G. [2006]. UWB radars for Bio-Medical Sensing: Attenuation Model for Wave Propagation in the body at 4GHz, *University of Trento Technical report DIT-06-051* .

[4] Blech, M. D. & Eibert, T. F. [2007]. A Dipole Excited Ultrawideband Dielectric Rod Antenna With Reflector, *IEEE Transactions on Antennas and Propagation* 55(7): 1948–1954.

[5] Buchegger, T., Ossberger, G., Reisenzahn, A., Hochmaier, E., Stelzer, A. & Springer, A. [2005]. Ultra-Wideband Transceivers for Cochlear Implants, *EURASIP Journal on Applied Signal Processing* 18: 3069–3075.

[6] CST [2011]. *CST MICROWAVE STUDIO®, User Manual.* Darmstadt, Germany.

[7] Dederer, J. [2009]. *Si/SiGe HBT ICs for Impulse Ultra-Wideband (I-UWB) Communications and Sensing*, Cuvillier Verlag, Göttingen, Germany.

[8] Dederer, J., Schleicher, B., Santos, F., Trasser, A. & Schumacher, H. [2007]. *FCC compliant 3.1-10.6 GHz UWB Pulse Radar using Correlation Detection*, Proc. IEEE MTT-S Int. Microw. Symp., Honolulu, HI, pp. 1471–1474.

[9] Dederer, J., Schleicher, B., Trasser, A., Feger, T. & Schumacher, H. [2008]. A Fully Monolithic 3.1-10.6 GHz UWB Si/SiGe HBT Impulse-UWB Correlation Receiver, *IEEE International Conference on Ultra-Wideband (ICUWB)*, Vol. 1, pp. 33–36.

[10] Devine, P. [2000]. *Radar Level Measurement: The User's Guide*, VEGA Controls.

[11] Fear, E. C., Hagness, S. C., Meaney, P. M., Okoniewski, M. & Stuchly, M. A. [2002]. Enhancing Breast Tumor Detection With Near-field Imaging, *IEEE Microwave Magazine* 3(1): 48–56.

[12] Fort, A., Desset, C., Ryckaert, J., Doncker, P. D., Biesen, L. V. & Wambacq, P. [2005]. Characterization of the ultra wideband body area propagation channel, *Ultra-Wideband, 2005. ICU 2005. 2005 IEEE International Conference on*, p. 6 pp.

[13] Gabriel, S., Lau, R. W. & Gabriel, C. [1996]. The dielectric properties of biological tissues: II. Measurements in the frequency range 10 Hz to 20 GHz, *Phys. Med. Biol.* 41: 2251.

[14] Hees, A., Hasch, J. & Detlefsen, J. [2008]. Characteristics of a Corrugated Tapered Slot Antenna with Dielectric Rod and Metallic Reflector, *IEEE International Conference on Ultra-Wideband*, Vol. 1.

[15] Hertel, T. W. [2005]. Cable-current Effects of Miniature UWB Antennas, *IEEE International Symposium on Antennas and Propagation*, Vol. 3A, pp. 524–527.

[16] Kidera, S., Sakamoto, T. & Sato, T. [2009]. High-Resolution 3-D Imaging Algorithm With an Envelope of Modified Spheres for UWB Through-the-Wall Radars, *Antennas and Propagation, IEEE Transactions on* 57(11): 3520–3529.

[17] Kidera, S., Sakamoto, T. & Sato, T. [2010]. Accurate UWB Radar Three-Dimensional Imaging Algorithm for a Complex Boundary Without Range Point Connections, *Geoscience and Remote Sensing, IEEE Transactions on* 48(4): 1993–2004.

[18] Krach, B., Lentmaier, M. & Robertson, P. [2008]. Joint bayesian positioning and multipath mitigation in gnss, *Acoustics, Speech and Signal Processing, 2008. ICASSP 2008. IEEE International Conference on*, pp. 3437–3440.

[19] Leberer, R. [2005]. *Untersuchung von quasi-planaren Antennen mit sektorförmiger und omnidirektionaler Strahlungscharakteristik im Millimeterwellenbereich*, Dissertation, Universität Ulm, Institut für Mikrowellentechnik.

[20] Leib, M. [2011]. *Ultrabreitbandige Antennen für Kommunikation und Sensorik in der Medizintechnik*, Dissertation, Universität Ulm, Institut für Mikrowellentechnik.

[21] Leib, M., Mach, T., Schleicher, B., Ulusoy, C. A., Menzel, W. & Schumacher, H. [2010]. Demonstration of UWB communication for implants using an energy detector, *German Microwave Conference, 2010*, pp. 158–161.

[22] Leib, M., Schmitt, E., Gronau, A., Dederer, J., Schleicher, B., Schumacher, H. & Menzel, W. [2009]. A compact ultra-wideband radar for medical applications, *Frequenz* 63(1-2): 2–8.

[23] Lin, D., Trasser, A. & Schumacher, H. [2011a]. *A Fully Differential IR-UWB Front-end for Noncoherent Communication and Localization*, Proc. IEEE ICUWB 2011, Bologna, Italy, pp. 116–120.

[24] Lin, D., Trasser, A. & Schumacher, H. [2011b]. *Low Power, Fully Differential SiGe IR-UWB Transmitter and Correlation Receiver ICs*, Proc. IEEE RFIC, Baltimore, MD, pp. 101–104.

[25] Merdes, C. L. & Wolf, P. D. [2001]. Locating a catheter transducer in a three-dimensional ultrasound imaging field, *Biomedical Engineering, IEEE Transactions on* 48(12): 1444–1452.

[26] Mirbach, M. & Menzel, W. [2011]. A simple surface estimation algorithm for UWB pulse radars based on trilateration, *ICUWB 2011, 2011 IEEE International Conference on Ultra-Wideband*, pp. 273–277.

[27] Mirbach, M. & Menzel, W. [2012]. Time of Arrival Based Localization of UWB Transmitters Buried in Lossy Dielectric Media, *ICUWB 2012, 2012 IEEE International Conference on Ultra-Wideband*, pp. 328–332.

[28] Rappaport, C. [2004]. A simple approximation of transmitted wavefront shape from point sources above lossy half spaces, *Geoscience and Remote Sensing Symposium, 2004. IGARSS '04. Proceedings. 2004 IEEE International*, Vol. 1, pp. 421–424.

[29] Sakamoto, T. [2007]. A fast algorithm for 3-dimensional imaging with UWB pulse radar systems, *IEICE Transactions on Communications* E90-B(3): 636–644.

[30] Schantz, H. [2005]. *The Art and Science of Ultra-Wideband Antennas*, Artech House, Norwood, USA.

[31] Schleicher, B. [2012]. *Impulse-Radio Ultra-Wideband Systems for Vital-Sign Monitoring and Short-Range Communications*, Verlag Dr. Hut, München, Germany.

[32] Schueppert, B. [1988]. Microstrip/Slotline Transitions: Modeling and Experimental Investigation, *IEEE Transactions on Microwave Theory and Techniques* 36(8): 1272–1282.

[33] Staderini, E. M. [2002]. UWB Radars in Medicine, *IEEE Aerospace and Electronic Systems Magazine* 17(1): 13–18.

[34] Thiasiriphet, T., Ibrahim, M. & Lindner, J. [2012]. *Compressed Sensing for UWB Medical Radar Applications*.

[35] Thiasiriphet, T. & Lindner, J. [2010]. An uwb receiver based on a comb filter with shortened delay, *Ultra-Wideband (ICUWB), 2010 IEEE International Conference on*, Vol. 1, pp. 1–4.

[36] Thiasiriphet, T. & Lindner, J. [2011]. Particle filtering for uwb radar applications, *Ultra-Wideband (ICUWB), 2011 IEEE International Conference on*, pp. 248–252.

[37] Thiasiriphet, T., Zhan, R. & Lindner, J. [2009]. Interference suppression in ds-ppm uwb systems, *Ultra-Wideband. ICUWB 2009. 2009 IEEE International Conference on*, pp. 718–722.

[38] Thiel, F., Hein, M., Schwarz, U., Sachs, J. & Seifert, F. [2008]. Fusion of Magnetic Resonance Imaging and Ultra-Wideband-Radar for Biomedical Applications, *IEEE International Conference on Ultra-Wideband*, Vol. 1, pp. 97–100.

[39] Zheng, Y., Wong, K., Asaru, M., Shen, D., Zhao, W., The, Y., Andrew, P., Lin, F., Yeoh, W. & Singh, R. [2007]. *A 0.18um CMOS Dual-Band UWB Transceiver*, IEEE ISSCC Dig. Tech. Papers, San Francisco, CA, pp. 114–115.

[40] Zhou, Z., Pan, Z. & Tang, X. [2007]. A new family of optimal zero correlation zone sequences from perfect sequences based on interleaved technique, *Signal Design and Its Applications in Communications, 2007. IWSDA 2007. 3rd International Workshop on*, pp. 195–199.